PHILOSOPHICAL TRANSACTIONS OF THE ROYAL SOCIETY A MATHEMATICAL, PHYSICAL & ENGINEERING SCIENCES

On the Dilatation of Synthetic Type Ib Diamond by Substitutional Nitrogen Impurity

A. R. Lang, M. Moore, A. P. W. Makepeace, W. Wierzchowski and C. M. Welbourn

Phil. Trans. R. Soc. Lond. A 1991 **337**, 497-520
doi: 10.1098/rsta.1991.0135

On the dilatation of synthetic type Ib diamond by substitutional nitrogen impurity

By A. R. Lang[1], M. Moore[2], A. P. W. Makepeace[3], W. Wierzchowski[2]† and C. M. Welbourn[4]

[1] *H. H. Wills Physics Laboratory, University of Bristol, Tyndall Avenue, Bristol BS8 1TL, U.K.*

[2] *Department of Physics, Royal Holloway and Bedford New College, University of London, Egham, Surrey TW20 0EX, U.K.*

[3] *Department of Physiology, School of Medicine, University of Bristol, Bristol BS8 1TD, U.K.*

[4] *Diamond Trading Company Ltd, DTC Research Centre, Belmont Road, Maidenhead, Berkshire SL6 6JW, U.K.*

Contents

Sequences of high-Bragg-angle ($\theta_B = 74°$) double-crystal X-ray topographs taken at the SRS (Daresbury, U.K.) have yielded precise measurements of lattice parameter differences between growth sectors of different crystallographic forms in a large undoped synthetic diamond whose type Ib infrared absorption spectrum (principal peak at 1130 cm^{-1}) indicated atomically dispersed nitrogen, singly substituting for carbon, as the only detectable impurity. The plate-shaped specimen, polished parallel to (110), $5.0 \times 3.2\,mm^2$ in area, 0.7 mm thick, possessed an unusually well-developed ($1\bar{1}0$) growth sector containing nitrogen impurity concentration of only *ca.* 10^{-6}, which served as an internal standard of pure-diamond lattice parameter

†Permanent address: Institute of Electronic Materials Technology, Wólczyńska 133, 01-919 Warsaw, Poland.

Phil. Trans. R. Soc. Lond. A (1991) **337**, 497–520
Printed in Great Britain

with which lattice parameters of nitrogen-containing growth sectors were compared. The specimen's suitability for precision diffractometry was checked by comprehensive tests using optical microscope techniques, cathodoluminescence and single-crystal X-ray topography. The double-crystal combination was silicon reference crystal, asymmetric 175 reflection, with diamond specimen symmetrical 440 reflection. The principal measurement was the increase of the lattice parameter, a_0, of the $(1\bar{1}1)$ growth sector (nitrogen content 88 ± 7 parts per 10^6 atomic) relative to that of the $(1\bar{1}0)$ sector: $\Delta a_0/\bar{a}_0 = 1.18 \pm 0.07 \times 10^{-5}$. In terms of measured infrared absorption coefficient at $1130\ \mathrm{cm}^{-1}$, this gives $\Delta a_0/\bar{a}_0 = (2.95 \pm 0.27) \times 10^{-6}[\mu(1130\ \mathrm{cm}^{-1})/\mathrm{cm}^{-1}]$, which is believed to hold for growth sectors of all crystallographic forms. Combination with the nitrogen assay findings of Woods, van Wyk & Collins (*Phil. Mag.* B **62**, 589–595 (1990)) provides a direct relation to c_N, the fractional atomic concentration of substitutional nitrogen, as $\Delta a_0/\bar{a}_0 = (0.14 \pm 0.02)c_N$, which indicates that the effective volume of a single substitutional nitrogen atom in diamond is 1.41 ± 0.06 times that of the carbon atom it replaces. This substantial dilatation conflicts with several models for the substitutional nitrogen structure.

1. Introduction

Experiments in recent years have demonstrated that both natural and synthetic diamonds can exist as nearly ideal perfect crystals, as judged by their long-range lattice perfection. This is tested by X-ray methods, which study the closeness of the observed X-ray diffraction behaviour to that predicted by the dynamical theory of X-ray diffraction by perfect crystals. In the case of natural diamond, a very close approach to perfect-crystal diffraction properties has been verified quantitatively in a specimen having an impurity content of about 1 part in 10^3 (Lang *et al.* 1991). With such specimens, lattice parameter determinations with a precision of 1 part in 10^6 are possible, and on a sufficiently well-characterized specimen will produce numbers that carry genuine scientific significance. Defects in diamond not associated with impurity but capable of affecting the lattice parameter are radiation damage and dislocations. That a specimen has a low dislocation density is easily checked by birefringence photography and X-ray topography. The question of radiation damage does not arise in synthetic diamonds of known history; and in natural diamonds the presence and distribution of such damage is sensitively revealed by cathodoluminescence topography (Hanley *et al.* 1977).

The dominant identified impurity in both natural and synthetic diamonds is nitrogen; and the standard classification of diamonds by optical properties, namely type I, type II and their sub-divisions (Dyer *et al.* 1965), is based upon those ultraviolet (UV), visible and infrared (IR) absorption characteristics of diamond that depend upon concentration and state of aggregation of nitrogen impurity (except in semiconducting type IIb diamonds, which are characterized by absorption due to uncompensated boron acceptor centres: for details see reviews of the optical properties of diamond by Davies (1977) and Walker (1979)). About 98% of natural diamonds contain sufficient nitrogen to cause substantial reduction in their UV transmission in the wavelength range 0.22 μm to 0.34 μm. In the great majority of these the nitrogen is present in states of aggregation that render the nitrogen impurity electron spin resonance (ESR) inactive; such diamonds belong to type Ia. In

PHILOSOPHICAL TRANSACTIONS OF THE ROYAL SOCIETY A MATHEMATICAL, PHYSICAL & ENGINEERING SCIENCES

a small minority of natural UV absorbing diamonds (about 0.1%) a significant fraction of the nitrogen impurity has not aggregated, but exists atomically dispersed, singly substituting for carbon atoms. In synthetic diamonds grown by the standard high-pressure, high-temperature procedures, and which have reasonable perfection, i.e. have low densities of dislocations and inclusions, all the nitrogen impurity is in the dispersed, substitutional state. Such nitrogen is identified by its characteristic ESR signal (Smith *et al.* 1959; Loubser & van Wyk 1978) and by its optical absorption spectrum, which properties identify the specimen as belonging to type Ib. The present work is concerned with synthetic diamond in this category.

When the identity and concentration of an impurity are known, and when (as in the present case) all evidence points towards it being present in one point-defect form only, the way is opened for meaningful comparison between observed lattice parameter change and that predicted to result from a population of point defects possessing specified atomic structure. For substitutional nitrogen in diamond there is agreement that the nitrogen is not ionized at room temperature and that the donor electron resides on one of the four nitrogen–carbon bonds surrounding the impurity atom. However, there is great disagreement concerning how much this unique nitrogen–carbon bond is lengthened relative to the standard interatomic distance in diamond: estimates range from 5% to 36% (and will be reviewed later, in §5*b*). The work here reported has established the relation between diamond lattice parameter increase and the strength of the principal infrared absorption known to be proportional to the concentration of substitutional nitrogen. By applying a recognized proportionality factor between nitrogen content and absolute strength of this absorption, such as that provided by the recent nitrogen assays of Woods *et al.* (1990), a figure for the effective volume of a substitutional nitrogen atom can be derived. This figure immediately puts some broad constraint on the range of possible local atomic structures surrounding the nitrogen atom, and in particular on the length of the unique nitrogen–carbon bond. To narrow this constraint materially requires calculations, yet to be performed, in which the atomic structure of the point defect is matched to a surrounding elastically deformed matrix; and it is hoped to report on this work in due course.

A striking characteristic of synthetic diamond is the strong dependence of nitrogen impurity incorporation on the crystallography of the growth surface. In particular, it is found that {110} growth facets very effectively reject incorporation of nitrogen. Consequently, a specimen containing well-developed {110} growth sectors in which the nitrogen content is negligible carries within it its own standard of pure diamond with which other growth sectors may be compared. This condition was exploited in the X-ray diffractometry, described in §4. A specimen unusually favourably grown with respect to the desired morphological features was chosen for the experiments, and is described in §2. Diamonds, both natural and synthetic, are remarkable for variety and inhomogeneity of lattice defect content. Consequently, an essential preliminary to the lattice parameter study was a comprehensive assessment of the specimen by a range of techniques, optical, X-ray and cathodoluminescence, so as to establish its suitability for diffractometry. These assessments are described in §3.

2. Specimen

Large single crystals of diamond, i.e. with diameters exceeding 3–4 mm, are grown by the reconstitution method in which the carbon source is fine diamond powder and

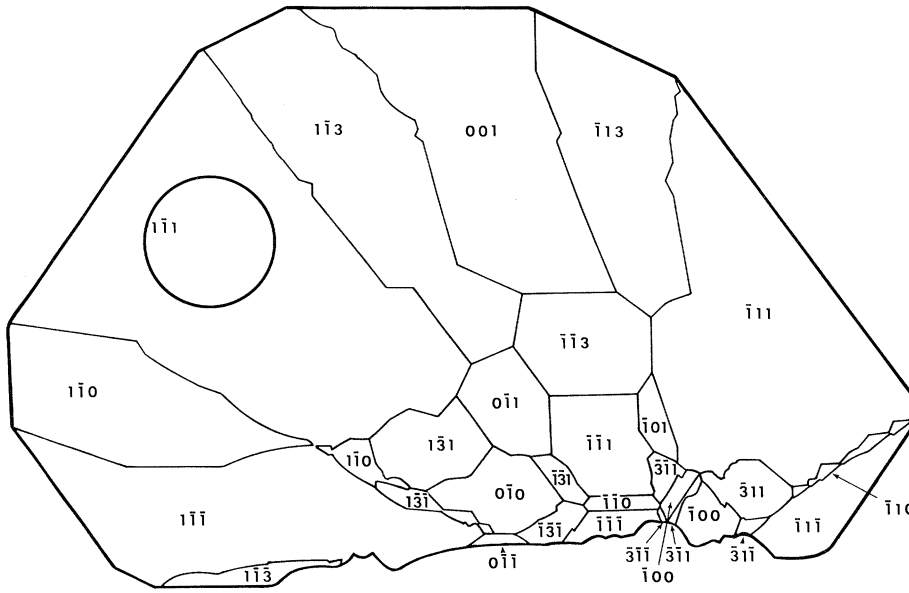

Figure 1. Map of growth sectors intersected by one polished surface of polished slice of synthetic diamond. Overall width 5 mm, mean thickness 0.7 mm, surfaces parallel within $\frac{1}{2}°$. The normal to the surface shown is close to the direction indexed [110], being tilted about 1.25° away from this direction towards [$\bar{3}$31]. The circle imposed on the (1$\bar{1}$1) growth sector outlines the 0.7 mm diameter area probed in the infrared absorbance measurement used in this work.

growth takes place on a limited number of seed crystals (Wentorf 1971; Strong & Wentorf 1972). Transfer of material from source to seed is by diffusion through carbon-saturated molten metal, and is driven by a temperature drop of about 30 °C from source to seed inside the high-pressure vessel, which is held at about 5.5 GPa and a mean temperature of about 1350 °C. The major habit forms of crystals grown under these conditions are {100} and {111}, roughly equally developed. Minor forms are {113} and {110}, which are highly variable in development, both from specimen to specimen and within a given specimen. For both optical and X-ray topographic experiments the most informative specimen shape is a central or near-central slice cut and polished parallel to (110). This intersects perpendicularly some growth facets of all forms {100}, {111}, {113} and {110}, and provides best conditions for detecting and quantitatively assessing impurity zoning (i.e. banding) in directions normal to these facets.

The specimen chosen for the present study came from a suite of large synthetic diamonds whose growth-sectorial-dependent optical properties have been described by Burns *et al.* (1990). This specimen (no. 1 in the suite) had been grown without any steps being taken to reduce nitrogen incorporation. It gave the standard type Ib IR absorption spectrum, with no evidence of any impurity other than nitrogen incorporated in the lattice; and all nitrogen was substitutional. Figure 1 is a complete map of the growth sectors intersected by one polished surface of the specimen, that surface used for X-ray reflection in the X-ray diffractometry experiments. It contains more detail than the partial growth sector map of this specimen shown in fig. 4 of Burns *et al.* (1990). In the map shown here the signs of indices are chosen so that the directions they indicate point in the direction of crystal growth. Thus, for example, the growth direction of the sector indexed ($\bar{1}\bar{1}$0) points into the specimen

plate, as viewed in figure 1. The evidence upon which the delineation and identification of growth sectors rests will emerge during descriptions of the figures following.

3. Assessment and growth sector mapping

(*a*) *Coloration*

The substitutional nitrogen in type Ib synthetic diamonds gives rise to an absorption in the visible spectrum that increases rapidly with decreasing wavelength below about 500 nm (Dyer *et al.* 1965). This imparts a yellow coloration to nitrogen-containing growth sectors. A colour photograph, fig. 2 of Burns *et al.* (1990), illustrates the visual appearance of the present specimen: deepest yellow in {111} growth sectors, {110} sectors colourless. Contrast between nitrogen-rich and nitrogen-poor regions is usefully enhanced by photographing through a blue-violet-transmitting filter, as shown by figure 2 here. Interpretation is clearest for those growth sectors whose facets lie in the [110] zone. In the lower central part of the specimen gradation of transmission arises from wedge-like overlap of more and less transmitting growth sectors. Figure 2 also shows the distribution of inclusions in the specimen. In the lower regions, which are closest to the seed crystal, the shadows of a few large and many small inclusions are seen, but inclusions become quite sparse in the upper peripheral zones of the slice.

It is evident that nitrogen concentration in the different growth sectors decreases in the sequence {111}, {100}, {113} and {110}. No visible absorption is detectable in the large $(1\bar{1}0)$ sector, left, and the narrow $(\bar{1}10)$ sector, right: they are water-white. Photographs such as figure 2 could be used for quantitative absorbance measurement and hence nitrogen determination if a calibrating optical density wedge were simultaneously exposed. The value of figure 2 in the present study is for assessing homogeneity of nitrogen incorporation in different growth sectors. Nitrogen concentration fluctuations in the {111} growth sectors are minor. In particular, there is no evident general gradient of nitrogen concentration in the outermost 1.5 mm of growth in the $(1\bar{1}1)$ sector. Thus the infrared absorption measurement embracing the circular area outlined in figure 1 provides a reliable average for that sector. On the other hand, the degree of zoning of nitrogen incorporation in the (001) sector is considerable. Of interest is the correlation between nitrogen content fluctuations in the various growth sectors. Close examination of the original micrograph film yields more detailed information than can be obtained from the print in figure 2, though the latter does reveal a few thin bands of lower nitrogen content that run continuously across growth sector boundaries, round from the $(1\bar{1}1)$ growth sector clockwise to the $(\bar{1}11)$ growth sector. In the $(1\bar{1}3)$ growth sector a survey of thin bands (thickness 50 μm to 150 μm) that contained more than that sector-average nitrogen content showed that whereas the majority joined up with corresponding bands of excess nitrogen in the (001) sector at the $(1\bar{1}3)/(001)$ sector boundary, a significant minority, about one third of the total, had no such correspondence.

(*b*) *Schlieren pattern*

The visual manifestations of refractive index inhomogeneities in transparent media are well known, and are put to practical use in Schlieren photography (Holder & North 1963). Diamond specimens having reasonably flat and smooth surfaces can be fruitfully examined by Schlieren techniques that can be realized with appropriate modification of an optical microscope. A set-up devised for detecting gradients of

PHILOSOPHICAL TRANSACTIONS OF THE ROYAL SOCIETY A MATHEMATICAL, PHYSICAL & ENGINEERING SCIENCES

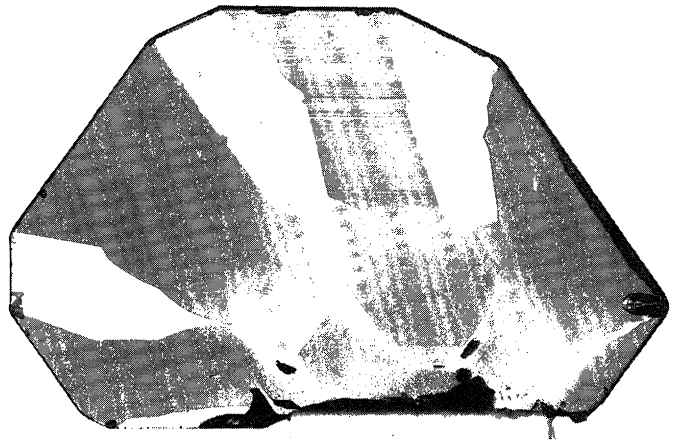

Figure 2. Transmission of visible light with illumination filtered to enhance contrast between nitrogen-rich sectors (dark) and sectors nitrogen-poor. Kodak-Wratten filter type 47B: peak transmittance 50% at 430 nm, falling to 1% at 380 nm and 490 nm. Orthochromatic film.

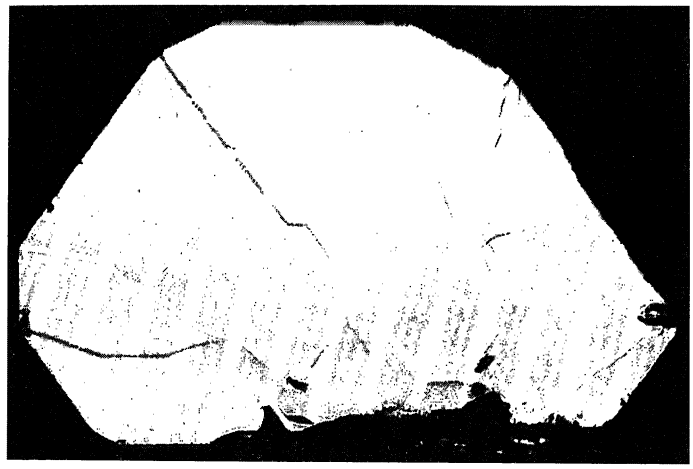

Figure 3. Variations in refractive index revealed by the Schlieren pattern.

nitrogen concentration in synthetic diamond (Frank *et al.* 1990) was used with the present specimen, yielding the pattern shown in figure 3. The optical arrangements combined collimated illumination, which showed up refractive index variations in any direction normal to the illuminating beam, together with a knife-edge system (Töpler 1866) consisting of an adjustable blade inserted close to the back focal plane of the microscope objective, which gave sensitivity to refractive index gradients perpendicular to the knife edge. Both near and far surfaces of the specimen (as viewed in figure 3) bear polishing striae running roughly parallel to [001], i.e. up and down in the figure. Orienting the knife edge horizontally has minimized contrast due to these striae in figure 3. From the sharpness of images of growth sector boundaries in figure 2 it can be seen which boundary segments lie most nearly normal to the polished surfaces of the specimen; and, as expected, these give most contrast in figure 3. Favourable boundary orientation plus relatively large changes in refractive index

PHILOSOPHICAL TRANSACTIONS OF THE ROYAL SOCIETY A MATHEMATICAL, PHYSICAL & ENGINEERING SCIENCES

combine to produce the bold contrast exhibited particularly by the $(1\bar{1}\bar{3})/(1\bar{1}\bar{1})$, $(1\bar{1}\bar{1})/(1\bar{1}0)$, $(1\bar{1}0)/(1\bar{1}1)$ and $(1\bar{1}1)/(1\bar{1}3)$ growth sector boundaries. In previous experiments it had been verified that substitutional nitrogen incorporation causes increase of refractive index. Whether a light or a dark band is produced at a given growth sector boundary is determined jointly by the direction of insertion of the knife blade and by tilting the illumination axis. Comparison of the growth banding patterns in figures 3 and 2 demonstrates that the Schlieren technique, though qualitative, is highly sensitive. It revealed no specimen inhomogeneities not attributable to variations in nitrogen content.

(*c*) *Infrared absorption*

Concentrations of substitutional nitrogen are inferred from the strength of absorption in the principal peak, at 0.14 eV, 1130 cm^{-1}, in the one-phonon absorption band characteristic of type Ib diamond. Spectra were recorded using a Bio-Rad (Digilab Division) Model FTS 40 Fourier transform IR spectrometer. For sampling selected small areas, measurements were made through a reflecting-objective microscope providing control of size, shape and orientation of sampled area (typically some tens of micrometres square). The results of such probing on the present specimen are given in table 1 of Burns *et al.* (1990). At probe positions located within the major growth sectors at a distance of about 0.4 mm from the faceted periphery of the specimen plate, absorption coefficients at 1130 cm^{-1}, given in units of cm^{-1} with uncertainty ± 0.1 cm^{-1}, are 3.99, 3.96, 1.85, 0.40 and 0.26 in the $(\bar{1}11)$, $(1\bar{1}1)$, (001), $(\bar{1}13)$ and $(1\bar{1}3)$ sectors respectively. For application in conjunction with X-ray diffractometry, re-measurement of absorption in the $(1\bar{1}1)$ sector has been performed. In this case the sampled area was defined by a 0.7 mm diameter circular aperture in contact with the specimen and located as shown in figure 1. The finding, 4.01 ± 0.13 cm^{-1}, agrees satisfactorily with that obtained with the smaller probe, and will be adopted as definitive for this sector. It was arrived at after subtracting the absorbance that would be produced by a similarly thick plate of ideal type IIa diamond, i.e. one both nitrogen-free and boron-free.

In the $(1\bar{1}0)$ growth sector the absorption at 1130 cm^{-1} was too weak to be measured. Burns *et al.* (1990) detail how nitrogen concentration in this sector was estimated via the UV absorption peak at 270 nm attributed to substitutional nitrogen, which is measurable in very thin or very low-nitrogen-concentration type Ib specimens. It was concluded that the $(1\bar{1}0)$ sector contained approximately one part per million substitutional nitrogen.

(*d*) *Cathodoluminescence topography*

A prime source of information leading to crystallographic identification of growth sectors intersected by polished diamond surfaces is the cathodoluminescence pattern. Diagnostic properties of the emissions are their spectral distribution and relative brightness, and their variations, often notable, with specimen temperature and current density of the impinging electron beam. The almost ubiquitous presence of growth bands with particular luminescence properties discloses the surface trace of the local growth facet. Furthermore, comparison of images obtained with electron beams of higher and lower depths of maximum generation of cathodoluminescence (say 4 μm for 40 keV electron energy and 0.5 μm for 10 keV in diamond) can reveal the direction of dip of growth bands and boundaries separating growth sectors possessing different luminescence properties, and sometimes allows rough measure-

PHILOSOPHICAL TRANSACTIONS OF THE ROYAL SOCIETY A MATHEMATICAL, PHYSICAL & ENGINEERING SCIENCES

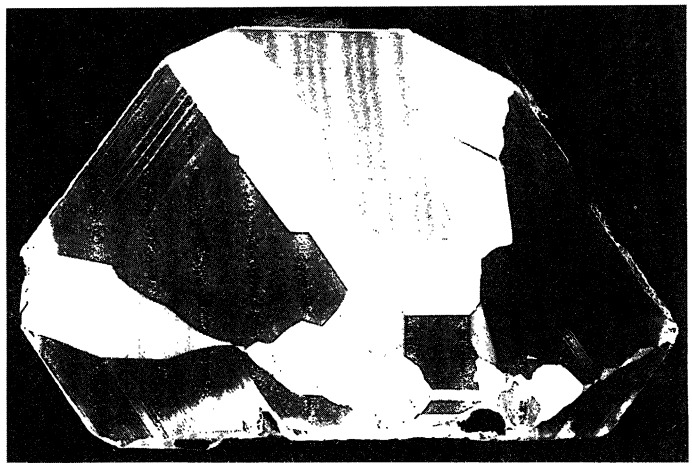

Figure 4. Room-temperature cathodoluminescence topograph of specimen surface indexed (110). Electron beam energy 40 keV, specimen current density *ca.* 1 μA mm^{-2}. Photographed through UV absorbing filter Kodak-Wratten 2B on to Kodak type 2415 extended red-sensitivity panchromatic film developed to give contrast (gamma) of *ca.* 1.

ment of dip angles. All such data helped in the preparation of the map in figure 1, especially in the case of small growth sector outcrops. The cathodoluminescence topograph (figure 4) was obtained by direct photography of the specimen surface flooded with a stationary electron beam. Various cathodoluminescence properties of this specimen have already been reported, namely the emission spectra from different growth sectors recorded at near liquid nitrogen temperature (Burns *et al.* 1990), and relations between the near IR 1.40 eV emission and the low-temperature green 2.56 eV emission from {111} sectors (Lang & Meaden 1991). The actual colours corresponding to the monochrome image (figure 4) are quite well reproduced in the colour photograph, fig. 3 of Burns *et al.* (1990). For a description of colours, including colour and relative brightness dependence upon electron beam current density, the account and tabulation in Woods & Lang (1975) is applicable also to this specimen. Briefly, at room temperature the colours are {113} blue-white, {110} steel blue, {100} green-yellow and {111} dark except for some green and reddish-brown bands. In the cathodoluminescence spectroscopy experiments, selected localities were excited using a scanning electron microscope probe raster covering an area of about 400 μm square, with flyback trace vertical in figure 4. Some residual radiation damage from this and other probes can be detected on figure 4. They produced diminished luminosity in $(1\bar{1}3)$ and $(\bar{1}13)$ sectors, and brighter blue emission in $(1\bar{1}0)$ and $(0\bar{1}1)$.

Including the 1.40 eV IR emission, some six different vibronic emission systems as well as several structureless bands can be recognized, taking all growth sectors together. None is yet properly understood. For none has proportionality with nitrogen content been established, or even association with nitrogen in some cases. However, it needs emphasizing that cathodoluminescence emission can be dominated by centres present in concentration of 10^{-8} or less, especially in the purer matrices where electron and hole diffusion lengths are longer and non-radiative recombination centres sparser. For the present purpose, the cathodoluminescence topographs offer indirect and qualitative confirmation of the homogeneity of impurity content in the {110}, $(1\bar{1}1)$ and $(\bar{1}11)$ growth sectors, and inhomogeneity in {113} and {100}.

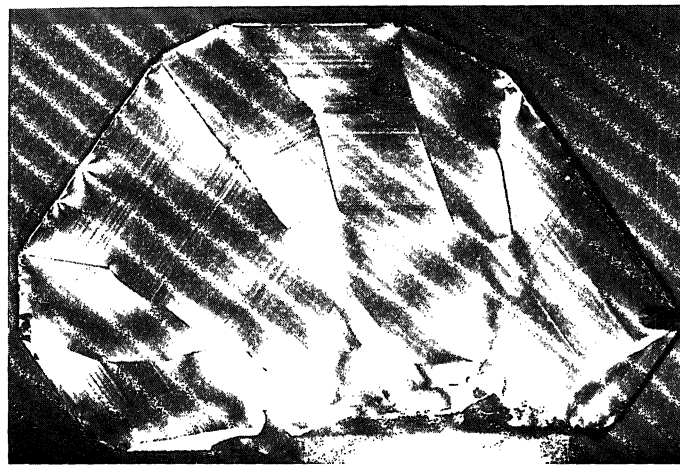

Figure 5. Birefringence pattern. Direction of view of specimen same as in figures 1–4. Axes of crossed polars parallel and perpendicular to $(\bar{1}13)$. (The specimen is supported at its lower edge by a bar of natural, plastically-deformed type IIa diamond 2 mm wide and 1 mm thick whose tip appears, strongly birefringent, at the bottom of the image.)

(*e*) *Strain birefringence*

Attention will now be turned to assessment techniques that reveal strain in the specimen. Observations of strain birefringence in diamond have a long history: notable studies being by G. Friedel (1924) and Ramachandran (1946). Recently it has been shown that individual dislocations and stacking faults in diamond can be detected by their birefringence images (Jiang *et al.* 1987; van Enckevort & Seal 1988). The birefringence pattern (figure 5) shows three sources of birefringence relevant to the present work. First are the birefringent laminae parallel to growth surfaces. These show up in all growth sectors where the growth surface is viewed edge-on, except for the $(1\bar{1}0)$ and $(\bar{1}10)$ sectors. They vanish when the axes of the crossed polars are set parallel and perpendicular to the growth surface concerned. The behaviour of the laminae as uniaxially birefringent, either positive or negative, with optic axis normal to the local growth surface, can be accounted for by elastic accommodation between growth layers possessing different cubic lattice parameters, but a contribution from 'grown-in' departures from cubic symmetry is possible. A second source of birefringence is long-range strain produced by growth sector boundaries, seen especially at boundary kinks. The third source of birefringence can be termed accidental, arising from burrs around the periphery of the plate, and, particularly strongly, from the larger inclusions near the bottom edges of the plate. (Birefringence can also reveal percussion damage and scratches, but these do not obtrude in figure 5.)

The absence of birefringent bands in the $(1\bar{1}0)$ sector provides sensitive confirmation of the homogeneity of this sector and is supporting evidence for its purity. The banded distribution of the blue cathodoluminescence centres in this sector, described in §3*d* above, gives rise to no detectable corresponding bands of strain birefringence. The birefringence pattern suggests in a qualitative way that the $(1\bar{1}0)$ sector is sufficiently large for lattice parameter measurements made on its central area to be not significantly perturbed by stresses at its boundaries with the adjacent $(1\bar{1}1)$ and $(1\bar{1}\bar{1})$ sectors.

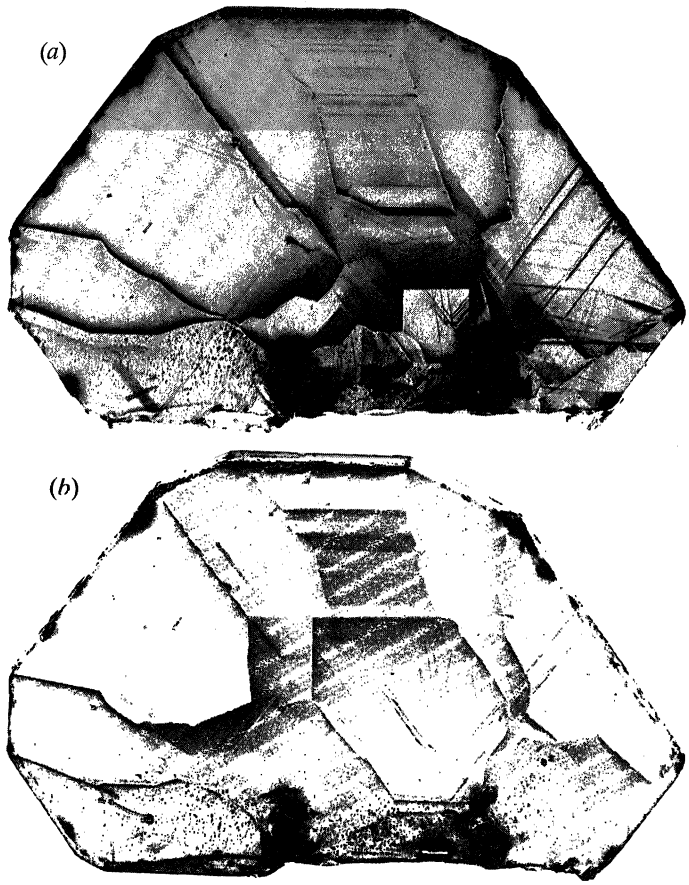

Figure 6. Reflection X-ray topographs of specimen surfaces, CuKα_1 radiation, $\lambda = 0.154$ nm, 331-type reflections, $2\theta_B = 140.5°$. Angle between incident beam and surface normal = 33°, and between surface normal and reflected beam = 6.5°. (*a*) Surface indexed (110), reflection 331. (*b*) Surface indexed ($1\bar{1}0$), reflection $\bar{3}3\bar{1}$ (printed reflected in (001) for comparison with (*a*) and other figures).

Stacking faults seen edge-on appear as light or dark lines depending upon the orientation of the polars and the background strain field in the surrounding matrix (Jiang *et al.* 1987). Thus, with the polars setting of figure 5, a stacking fault parallel to ($1\bar{1}1$) appears as a fine white line in the ($1\bar{1}\bar{1}$) sector, whereas a set of similarly oriented faults in the ($\bar{1}11$) sector appear as dark lines. Other linear birefringent features appearing in figure 5 may be dislocations or trajectories of corners of growth sectors: that can be discovered by X-ray topography.

(*f*) X-*ray reflection topography*

Surface reflection X-ray topographs reveal outcrops of dislocations and growth sector boundaries and are sensitive to surface damage. Furthermore, the strength of integrated reflection from an area free from individually resolvable images of defects provides a statistical measure of lattice perfection in that area, lower integrated reflection implying higher perfection. Examples of X-ray reflection topographs used in conjunction with optical micrography and cathodoluminescence topography of polished surfaces of natural diamond appear in Lang (1974). A diamond (110) surface

can be imaged almost free from geometric distortion using CuKα_1 radiation and reflections 331 or 33$\bar{1}$. Figure 6*a*, *b* shows such images of the specimen surfaces indexed (110) and ($\bar{1}\bar{1}$0) respectively. Some features already seen in figures 2–5 can be recognized, differently manifested. Others, such as dislocations, are obviously best detected by X-ray topography. The combination of X-ray wavelength and diffraction geometry chosen ensures that features producing diffraction contrast on the remote surface of the specimen are also visible, albeit weakly compared with corresponding images on the near, X-ray reflecting, surface. Area contrast from growth sector boundaries within the interior of the crystal is evident in many cases. Thus the three-dimensional geometry of growth sectors is disclosed. For example, comparison of figure 6*a*, *b* shows the considerable expansion of the ($\bar{1}\bar{1}$1) sector in going from its section in figure 6*a* to that in figure 6*b*. Stereopairs of X-ray topographs can be obtained by making a specimen rotation about the diffraction vector between exposures, 7.5° being an appropriate angle for the 331-type reflections. Viewing such pairs with twin microscopes gives a stereoscopic effect dramatic as well as informative, revealing, for example, the trajectories of dislocations and distribution of inclusions within the specimen volume.

Except for the (001) sector, little diffraction contrast due to growth banding is seen. Strong contrast is generated by the strain fields of inclusions in the lower part of the specimen, but does not extend at all significantly into the (1$\bar{1}$0) and (1$\bar{1}$1) sectors important in the X-ray diffractometry experiments. Stacking faults in the ($\bar{1}$11) sector and elsewhere are visible, but are absent in the (1$\bar{1}$0) and (1$\bar{1}$1) sectors. There is fortunately little mechanical damage producing diffraction contrast on the polished surfaces: most obvious is a pair of long scratches crossing the (1$\bar{1}$1), (1$\bar{1}$3) and ($\bar{1}$1$\bar{3}$) sectors on the (110) surface (figure 6*a*). The topographs do not detect a higher integrated reflection from sectors of higher nitrogen content. The image in figure 6*a*, and to a lesser degree that in figure 6*b*, provide essential reference patterns with which to compare the double-crystal topograph images shown below.

4. X-ray diffractometry

(*a*) *Methods applicable*

A description of the method chosen and of its practical implementation can usefully be introduced by viewing it in the general context of methods for measuring and mapping lattice parameters (Hart 1981). Absolute measurements of lattice parameter (a_0) do not necessarily involve greater instrumental complexity than relative measurements. Two very different methods, the divergent-beam (Kossel) method (Lonsdale 1947) and the single-crystal X-ray goniometry method developed by Bond (1960), measure the ratio λ/a_0 directly, and thus relate a_0 to an X-ray emission line standard. The best-known lattice parameter measurements on single-crystal diamonds have been made by these two methods (Lonsdale 1947; Kaiser & Bond 1959). All methods involving X-ray goniometry rely on the use of high Bragg angles to obtain high sensitivity in measurement of interplanar spacing, d, as the differential form of Bragg's Law shows:

$$\Delta d/d = \Delta\lambda/\lambda - \cot\theta_B\,\Delta\theta_B. \tag{1}$$

The small unit cell size of diamond, $a_0 = 0.3567$ nm, restricts the number of reflections observable at large Bragg angles with longer wavelengths such as the most frequently used characteristic radiation, CuKα_1, $\lambda = 0.154$ nm. Use of the continuous

spectrum provided by synchrotron radiation removes this restriction, but requires the wavelength diffracted to be defined. Definition can be achieved by multiply reflecting the X-ray beam between appropriately cut surfaces on a silicon crystal so as to obtain two or more successive reflections from non-parallel Bragg planes having different d-spacings. Beams with wavelengths such as 0.140 nm, 0.135 nm (Ando *et al.* 1989), and 0.124 nm (Petroff *et al.* 1980), extremely well-collimated (exit beam divergence down to a few microradians) and spectral pass-band less than 10^{-5} (more than an order of magnitude narrower than the CuKα_1 emission line width) have been selected this way; and applied with the Bond method would serve well for absolute determination of a_0 of diamond specimens in terms of a standard silicon spacing. However, as explained previously, the aim of the present experiments was to measure the difference in lattice parameter between {110} sectors and nitrogen-containing sectors in the specimen. This comparison was achieved with a long-established double-crystal topographic technique (Bond & Andrus 1952) adapted to record reflections at high Bragg angles. This technique uses the parallel, or $(+-)$, setting of reference and specimen crystals (Compton & Allison 1935). A sequence of reflection topographs of the specimen surface is obtained in a step-wise sweep through the angular range over which the specimen crystal reflects rays impinging on it from the (perfect) reference crystal after Bragg reflection by the latter. If both crystals are Bragg-reflecting from planes with identical spacing, the parallel setting is dispersionless and the angular range of double-crystal reflection (the 'rocking curve') is free from broadening due to wavelength spread in the radiation incident on the reference crystal. If no reference crystal of similar species and of sufficient size and perfection is available (as in the present circumstances) then a near-matching spacing in a perfect crystal such as silicon has to be used. Fortunately, with the collimating conditions prevailing at the Synchrotron Radiation Source, lack of perfect d-match imposed entirely negligible penalties, as explained in §5*a* below.

At what angular position on the rocking curve a particular region of the specimen reflects depends upon its 'effective tilt', which contains components due to both local rotation and dilatation (Bonse 1958). Separation of these components is achieved as follows (Bonse 1965; Kikuta *et al.* 1966). Consider two regions in the specimen, 1 and 2, that have slightly different interplanar spacings, d_1 and d_2 (with mean $\bar{d}$), and slightly differently oriented Bragg-plane unit normals $\hat{\boldsymbol{g}}_1$ and $\hat{\boldsymbol{g}}_2$. Assume the dispersionless condition. Assume also that the direction of rays incident on the specimen crystal and the mean Bragg-plane normal $\hat{\bar{\boldsymbol{g}}}$ are both perpendicular to the axis (direction $\hat{\boldsymbol{\omega}}$) about which the specimen rotation, ω, is made. Suppose angular settings for peak reflection from regions 1 and 2 are ω_{P} (1) and ω_{P} (2) respectively, ω increasing in the direction θ_{B} increasing. Then, making use of (1),

$$\Delta\omega \equiv \omega_{\mathrm{P}}(1) - \omega_{\mathrm{P}}(2) = [(d_2 - d_1)/\bar{d}]\tan\theta_{\mathrm{B}} + \hat{\boldsymbol{g}}_1 \times \hat{\boldsymbol{g}}_2 \cdot \hat{\boldsymbol{\omega}} \tag{2}$$

Let the specimen be mounted on a 'vertical' circle (or χ-circle) whereby it can be rotated about $\hat{\bar{\boldsymbol{g}}}$ to angular setting χ. Change of χ by 180° changes the sign of $\hat{\boldsymbol{\omega}}$ with respect to $\hat{\boldsymbol{g}}_1 \times \hat{\boldsymbol{g}}_2$. Combining peak-angle difference measurements at $\chi = 0°$ and $\chi = 180°$ gives the sought interplanar spacing difference,

$$(d_2 - d_1)/\bar{d} = \tfrac{1}{2}\cot\theta_{\mathrm{B}}[\Delta\omega(0°) + \Delta\omega(180°)]. \tag{3a}$$

The orientation difference between $\hat{\boldsymbol{g}}_1$ and $\hat{\boldsymbol{g}}_2$ can be found from

$$\hat{\boldsymbol{g}}_1 \times \hat{\boldsymbol{g}}_2 \cdot \hat{\boldsymbol{\omega}} = \tfrac{1}{2}[\Delta\omega(0°) - \Delta\omega(180°)] \tag{3b}$$

taken together with another pair of measurements such as $\Delta\omega$ (90°) and $\Delta\omega$ (270°).

(*b*) *Experimental arrangements*

A reflection from planes parallel, or nearly parallel, to the specimen surface was desired so that the interplanar spacing parallel to a free surface could be measured and images little distorted from the view normal to the specimen surface would be recordable at any azimuthal angle, χ. Narrower rocking curves are produced by shorter wavelengths and higher-order reflections, but the best combination of synchrotron radiation output, topographic resolution of defects producing diffraction contrast and photographic emulsion recording properties is obtained at wavelengths not lower than 0.1 nm. The symmetric 440 reflection from the specimen surface satisfied the above requirements, with the added great advantage of a good d-match with the silicon 175 reflection (diamond 440, $d = 0.1261$ nm; silicon 175, $d = 0.1254$ nm; relative mismatch 0.54%). In symmetrical Bragg reflection a perfect non-absorbing crystal is totally reflecting over the angular range $\Delta\theta_{\mathrm{tot}}$ given by

$$\Delta\theta_{\mathrm{tot}} = 2r_{\mathrm{e}}\, d|F_g|\lambda C/\pi V \cos\theta_{\mathrm{B}}, \tag{4}$$

in which r_{e} is the classical radius of the electron, F_g is the structure factor of the reflection at the temperature of observation, V is the unit cell volume and C is the polarization factor (which was 1 in the present experiments, the plane of incident and diffracted rays being vertical, normal to the plane of the synchrotron storage ring). Outside the range of total reflection, the reflectivity, $R(\Delta\theta)$, falls off as

$$R(\Delta\theta) = 1 - [1 - (\Delta\theta_{\mathrm{tot}}/2\Delta\theta)^2]^{\frac{1}{2}}, \tag{5}$$

the angle $\Delta\theta$ being measured from the centre of the range of total reflection. Absorption causes a lowering and rounding of the reflectivity curve; and skewness develops, more pronounced the greater the magnitude of the fraction $\epsilon = F_g''/F_0''$, the ratio of the imaginary parts of the structure factor for orders g and 0. Reflectivity curves for the absorbing case may be computed from equations (16) and (19) of Hirsch & Ramachandran (1950), using theoretical values of ϵ calculated by Hildebrandt *et al.* (1975).

Equation (4) shows that for fixed λ and d, $\Delta\theta_{\mathrm{tot}}$ is proportional to $|F_g|/V$, which quantity is 201 nm^{-3} for the diamond 440 and 100 nm^{-3} for the silicon 175 reflections, indicating that when both crystals are symmetrically Bragg reflecting the double-crystal rocking curve width will be dominated by the diamond reflection curve width. Further improvement in the ratio of reflection curve widths is obtained by asymmetric reflection at the silicon monochromator surface, using Bragg planes inclined at angle α to the surface. If the monochromator is set in the orientation that makes the glancing angle of incidence equal to $(\theta_{\mathrm{B}} - \alpha)$, the conventional 'asymmetry factor', b, has magnitude $|b| = \sin(\theta_{\mathrm{B}} - \alpha)/\sin(\theta_{\mathrm{B}} + \alpha)$. Then the ratio of spatial width of the reflected beam to that of the incident beam is $1/|b|$, and the angular width of totally reflected rays in the reflected beam is reduced to $|b|^{\frac{1}{2}}\Delta\theta_{\mathrm{tot}}$. A silicon monochromator with surface prepared parallel to (110), within *ca.* $\frac{1}{2}°$, was oriented so that the (175) planes, $\alpha = 49.22°$, were Bragg reflecting with glancing angle of incidence $(\theta_{\mathrm{B}} - \alpha)$, giving $|b| < 1$. Table 1 lists some parameters associated with this monochromator and specimen combination, calculated for a range of high Bragg angles that were experimentally accessible. Bragg angles of the monochromator and diamond specimen are θ_{M} and θ_{D} respectively. The horizontal incident beam is deviated through $2\theta_{\mathrm{M}}$ in the vertical plane by the monochromator (deviation upwards in practice) and the wavelength selected is $\lambda_{\mathrm{M}} = 2d_{\mathrm{M}} \sin\theta_{\mathrm{M}}$. For this

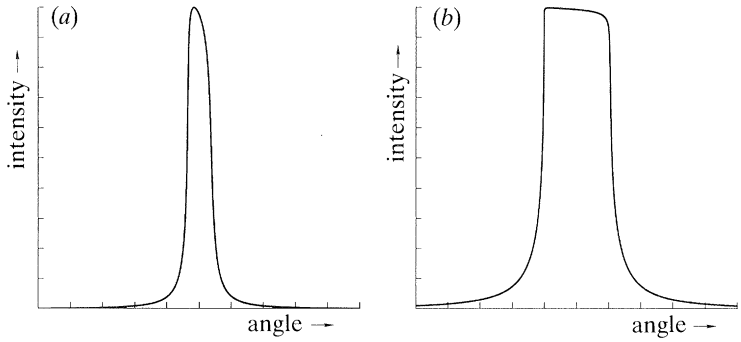

Figure 7. Computed single-crystal reflectivity curves, $\lambda = 0.121$ nm. Peaks normalized to unit height, abscissa scale divisions 1 arcsec. (*a*) Silicon, asymmetric 175 reflection, $|b| = 0.526$, $F(175) = 15.98$ (Saka & Kato 1986), normal linear absorption coefficient, $\mu = 70\ \mathrm{cm}^{-1}$, $\epsilon = 0.51$. (*b*) Diamond, symmetric 440 reflection, $F(440) = 9.14$ (Dawson 1967), $\mu = 8.2\ \mathrm{cm}^{-1}$, $\epsilon = 0.83$.

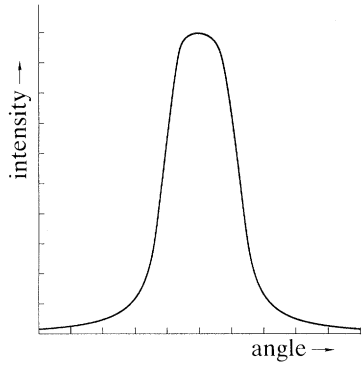

Figure 8. Convolution of reflectivity curves figure 7*a*, *b*. Peak normalized to unit height, abscissa scale divisions 1 arcsec. Full width at half maximum intensity (FWHM) equal to 2.44 arcsec.

Table 1. *Diffraction parameters dependent upon monochromator deviation angle* $2\theta_M$ *in the silicon* 175, *diamond* 440 *double-crystal arrangement*

(Parameters are explained in the text.)

$2\theta_M$/deg	128	135	145	150
λ_M/nm	0.1127	0.1159	0.1196	0.1211
θ_D/deg	63.35	66.74	71.52	73.86
$\tan\theta_D$	1.993	2.327	2.992	3.455
$(\theta_M - \theta_D)$/deg	0.64	0.76	0.98	1.14
$\lvert b\rvert^{-1}$	3.60	2.85	2.15	1.90
$\lvert b\rvert^{\frac{1}{2}}$	0.527	0.593	0.682	0.725
$\lambda_M \sec\theta_M \lvert b\rvert^{\frac{1}{2}}$/nm	0.151	0.194	0.284	0.339

wavelength the diamond Bragg angle is θ_D. The bottom row in table 1 combines the wavelength-dependent part of (4) with the asymmetry factor to give a 'probe angular width factor'. Choice of operating conditions involves a compromise, balancing increase of probe angular width against increase of $\tan\theta_D$ as $2\theta_M$ increases.

Figure 7*a*, *b* shows computed single-crystal reflectivity curves for monochromator and specimen, respectively, and figure 8 their convolution, the ideal double-crystal 'rocking curve', for the wavelength 0.121 nm. A useful indicator of the sensitivity of

the arrangement is the 'flank sensitivity' of the rocking curve, usually taken as the angular displacement of the curve that would produce a 10% change in reflected intensity at the steepest portion of the curve. This is 0.11 arcsec in figure 8.

Two series of diffractometry experiments were done at the SRS, Daresbury, the first at Station 9.4, on the 'wiggler' line, 36 m from the tangent point on the storage ring, the second at Station 7.6, 80 m from the tangent point. At both stations similar double-crystal cameras were available (Bowen & Davies 1983). Alignment of specimen and monochromator on these cameras was accomplished by optical aids supplemented by X-ray silhouetting experiments, an important optical component being a pinhole-collimated laser beam parallel with the incident X-ray beam. Large, permanently attached, slit boxes on the cameras prevented attainment of Bragg angles as high as would have been desirable. Use of a full 360° χ-circle had to be abandoned to reach usefully high angles. To replace the χ-circle an axially-slim frame was constructed having mirror symmetry in the median plane of incident and diffracted X-rays. To this frame the specimen-carrying goniometer head could be attached in either the $\chi = 0°$ or $\chi = 180°$ positions. Correct alignment of the specimen on its goniometer head, and of the rotational settings of the latter in its two positions in the frame, constituted essential preliminary work, done with conventional optical and X-ray goniometry away from the SRS. For the synchrotron radiation experiments a remotely controlled travelling plate cassette enabled most, if not all, of the needed sequence of exposures to be registered on one plate and/or film pack.

(*c*) *Observations and measurements*

The first double-crystal topographic observations showed that warping of the specimen due to inter-growth-sectorial coherency strains and to strain fields of the larger inclusions was less than anticipated. The mean misorientation between the left-hand and right-hand ends of the specimen (as viewed in the figures) was not more than 1 arcsec. This favourable situation, coupled with the particular configuration of the growth sectors of prime interest, ensured that azimuthal settings at only one pair of χ-values were sufficient to give all data needed for the lattice parameter comparison. In the experiments at Station 9.4 the high wiggler-line intensity allowed acquisition of double-crystal topographs of best resolution as far as photographic emulsion characteristics were concerned. Figure 9 shows members of such a sequence, recorded with $2\theta_{\mathrm{M}} = 128°$. The Ilford nuclear emulsion plates were given brief development, and the maximum optical density in the areas of uniform strong diffracted intensity was about 0.8. Geometrical resolution was limited by axial divergence. Taking the source FWHM in the axial direction (the electron orbit plane) as 2.3 mm, and with source-to-specimen and specimen-to-plate distances 36 m and 45 mm respectively, axial divergence causes an image axial spread somewhat under 3 μm.

In interpreting the patterns in figure 9*a–d* it is necessary to distinguish effects due to accidental strain, to deformations associated with growth sector boundaries, and to the lattice parameter differences. Among the first-mentioned, scratches on the specimen are rather more evident than in the single-crystal topographs (figure 6*a*, *b*); and they show either dominantly excess or dominantly deficiency of diffracted intensity depending on angular position on the rocking curve. One surface artefact requires explanation. The cathodoluminescence examinations left a thin, very hard, strongly adhering carbonaceous film on the diamond surface. This is removable by

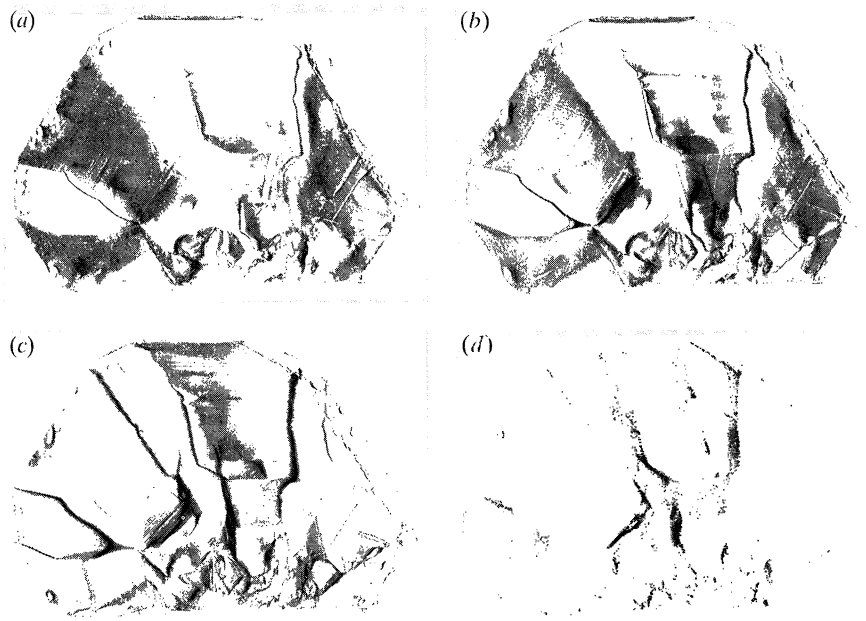

Figure 9. Members of a sequence of double-crystal topographs; silicon 175, diamond 440 reflection combination. $2\theta_M = 128°$, $\lambda = 0.113$ nm. Specimen glancing angle ω increasing in *ca.* 1 arcsec steps from (*a*) to (*d*). Azimuthal angle $\chi = 180°$, in which setting the plane of incidence is (001) and the diffracted beam leaves the crystal in a direction rotated 25.5° from the surface normal towards $[\bar{1}10]$ (allowing for $\approx 1°$ difference between [110] and the surface normal). Horizontal foreshortening factor 0.9. Ilford nuclear plates type L4, exposures *ca.* 100 mA minutes electron beam current.

Table 2. *Measurements of differences between angular settings for peak reflection from* $(1\bar{1}0)$ *and* $(1\bar{1}1)$ *growth sectors, diamond* 440 *reflection, wavelength* 0.121 *nm*

film no.	3	05	09	97	1	5	1*	5*	3*	7*
χ/deg	0	0	0	0	0	0	180	180	180	180
ω increasing (+) or decreasing (−)	+	+	+	+	−	−	+	+	−	−
$[\omega_P(1\bar{1}0) - \omega_P(1\bar{1}1)]$/s (nominal)	8.1	8.3	8.3	8.2	8.5	9.0	8.4	9.0	8.6	8.6
mean of repeated scans		8.2 (2)			8.7 (5)		8.7		8.6	
mean of positive and negative scans			8.4 (9)					8.6 (5)		
mean of $\chi = 0°$ and $\chi = 180°$ scans					8.5 (7)					

treatment in a hot oxidizing acid mixture. In the present case it was believed to have been adequately removed by mechanical scraping, but the double-crystal topographs revealed that removal had been incomplete. Variations in thickness of the adhering film remaining caused variations in the stress it applied to the diamond substrate. These variations are detectable in images of the $(1\bar{1}0)$ growth sector, which is free from images of growth banding. They appear in figure 9*d* as a 'brush stroke' pattern, running roughly from lower left to upper right, which was the principal direction of scraping.

When comparing figure 9*a–d* with the earlier figures, the somewhat oblique view of the specimen plate in these double-crystal topographs needs to be taken into

Figure 10. Sequences of double-crystal topographs recorded with $2\theta_M = 150°$, $\lambda = 0.121$ nm, ω increasing in nominal 1 arcsec steps from top to bottom. Recorded on Agfa-Strukturix D7 film, exposures *ca.* 70 mA minutes. (*a*) $\chi = 180°$, diffraction geometry similar to figure 9, but view of specimen surface less oblique (film 1*). (*b*) Repeat of (*a*) (film 5*). (*c*) $\chi = 0°$, image rotated 180° in its own plane for comparison with (*a*) and (*b*), so that the specimen viewing direction is from left of the surface normal (film 1). (*d*) Repeat of (*c*) (film 5).

PHILOSOPHICAL TRANSACTIONS OF THE ROYAL SOCIETY A MATHEMATICAL, PHYSICAL & ENGINEERING SCIENCES

account. Thus in the case of a feature running perpendicularly between the near and far surfaces of the specimen, the images in figure 9 show its far-surface outcrop displaced 0.3 mm to the right of its near-surface outcrop, i.e. by $\frac{1}{15}$ of the apparent width of the whole specimen surface. Examples are the displacements between the strong, near-surface and weak, far-surface images of $(1\bar{1}0)/(1\bar{1}1)$ and $(\bar{1}13)/(\bar{1}11)$ growth sector boundary outcrops. Regarding lattice parameter differences, figure 9*a* shows the $(1\bar{1}1)$ sector and most of the $(1\bar{1}\bar{1})$ sector near peak reflection. The (001) sector is reflecting in figure 9*c*, *d*. In (*d*) the $(1\bar{1}3)$, $(\bar{1}13)$ and $(1\bar{1}0)$ sectors are approaching their peaks. Down the central strip of the specimen the situation is complicated by overlap of growth sectors. Thus in figure 9*d* the outcrop of the $(\bar{1}\bar{1}3)$ sector on the near surface is strongly reflecting (and revealing scratches on that surface), whereas in 9*b* the strong reflection in the same image area comes from the expanding $(\bar{1}\bar{1}1)$ sector that lies below the $(\bar{1}\bar{1}3)$ sector. A significant anomaly exists in the lower right-hand region of the $(1\bar{1}\bar{1})$ sector, where these and other double-crystal topographs show less dilatation than the {111}-sector average. Here there is also somewhat less visible coloration (figure 2) and striking intense cathodoluminescence (figure 4), visually green and white.

Though informative on diffraction-contrast phenomena, the double-crystal topographs obtained on the high-intensity wiggler line were unreliable for lattice parameter comparison. Significant angular drifts attributable to beam-heating effects occurred during the time taken, say 10 to 15 min, to record a sequence of topographs. Values of $\omega_{\mathrm{P}}(1\bar{1}0)-\omega_{\mathrm{P}}(1\bar{1}1)$ obtained at $2\theta_{\mathrm{M}} = 128°$ ranged from about 3.5 to 5.5 arcsec; figure 9 illustrates part of a sequence with the lower value. Transfer of the experiments to Station 7.6, where the beam intensity at $\lambda \approx 0.1$ nm was over an order of magnitude lower, provided greatly improved stability, and confidence could be placed on the sequences recorded. Anticipating that irregularities in mechanical movements might lead to differences between actual and indicated ω-values ranging up to about $\frac{1}{2}$ arcsec, probe angular narrowness was sacrificed so as to gain a higher value of $\tan\theta_{\mathrm{D}}$. The highest possible $2\theta_{\mathrm{M}}$, 150°, allowed by mechanical limits was used in this second series of experiments. To compensate for loss of X-ray intensity, records were made on a fast, relatively coarse-grain film, which was given longer than normal development. Judging proximity to peak reflection settings involved integrating photographic density over areas large enough to render film granularity unobtrusive. Despite development to high contrast, the peak density in important areas did not exceed *ca.* 1, so that sensitivity to changes in intensity of X-rays by visual assessment was maintained. To allow for angular drifting, if present, rocking curves were recorded in pairs, ω increasing and ω decreasing, with minimum delay between the scans. Each pair was repeated. Ten scans covering the required angular range were recorded in steps of nominal size 1 arcsec. The findings (in number of steps) appear in table 2. Since the ω axis moved only 0.985 arcsec in response to a 1 arcsec step command, 8.5(7) steps means $\Delta\omega = 8.4(4)$ arcsec.

The important sections of four sequences are reproduced in figure 10 to show how the patterns recorded at $\chi = 0°$ and $\chi = 180°$ differ, and also how lack of reproducibility manifested itself. The position on the rocking curve at which it was chosen to commence photographic recording was always set at an integer on the ω scale of arcsec. However, through numerous repetitions of scans the sequence of patterns with ω-steps finer than 1 arcsec was built up because true starting points were randomly staggered as a result of drifts during the course of experimentation. This additional information helped in judging the probable

PHILOSOPHICAL TRANSACTIONS OF THE ROYAL SOCIETY A MATHEMATICAL, PHYSICAL & ENGINEERING SCIENCES

positions of peak reflections when they lay between adjacent exposures, and was applied in estimating to 0.1 arcsec the values of $\Delta\omega = \omega_P(1\bar{1}0) - \omega_P(1\bar{1}1)$. Assessment of the reliability to be attributed to the value of $\Delta d/d = -\Delta\omega \cot\theta_D$ obtained from the final average $\Delta\omega$ in Table 2 is discussed below. This average corresponds to $[a_0(1\bar{1}1) - a_0(1\bar{1}0)]/\bar{a}_0 = 1.18 \times 10^{-5}$. Regarding other growth sectors, similar averaging gave relative differences of a_0 from that of the $(1\bar{1}0)$ sector as 0.8×10^{-6} and 0.7×10^{-6} for the $(1\bar{1}3)$ and $(\bar{1}13)$ sectors respectively. In the case of the (001) sector, the relative lattice parameter differences from the $(1\bar{1}0)$ sector were apparently *ca.* 6.6×10^{-6} in the inner and *ca.* 4.0×10^{-6} in the outer zones.

5. Discussion

(*a*) *Accuracy of the diffractometry*

Sources of error in the measurement of $\Delta d/d$ can be categorized as (i) diffraction-geometrical factors familiar in single-crystal and double-crystal diffractometry, which can be closely estimated, (ii) mechanical irregularities and thermal drifts, and (iii) uncertainties in assessing topographic images. Factors in category (i) have been analysed by Bond (1960) and Compton & Allison (1935), and re-examined in many subsequent works. It is noteworthy that some geometrical factors that assume significance when conventional laboratory X-ray sources are used become completely negligible with the long specimen-to-source distance of 80 m at Station 7.6 at the SRS. The 'specimen crystal tilt error' and 'axial divergence error' discussed by Bond (1960) can be treated together for present purposes in the following way. If a ray incident upon the diamond specimen from the monochromator is normal to the specimen rotation axis (ω axis), as it correctly should be, but the specimen diffraction vector $\boldsymbol{g}$ is tilted by a small angle β out of the plane normal to the ω axis then $\sin\theta_B = (1 - \frac{1}{2}\beta^2)\sin\theta'_B$, where θ_B and θ'_B are the true and apparent Bragg angles respectively. In the setting-up procedure adopted the beam reflected from the monochromator was set perpendicular to the ω axis with an accuracy of between 0.1° and 0.2°. The optical and X-ray methods used to adjust the specimen crystal ensured that its mean $\boldsymbol{g}$ was not more than 0.1° to 0.2° off perpendicularity to the ω axis. Suppose these two errors combined adversely to make $\beta = 0.3°$, say, making $\frac{1}{2}\beta^2 = 1.4 \times 10^{-5}$. This would introduce serious error in absolute d-spacing measurements, but is of no consequence in the present measurement of d-spacing differences within the same specimen, which suffers from misorientations of no more than a few seconds of arc. However, d-spacing comparisons are made between points in the specimen separated by a distance h in the axial direction. These points reflect X-rays diverging from the source at distance $a = 80$ m, the axial divergence between them being $\beta_h = (h/a)$. The maximum h applying in the comparison between the $(1\bar{1}0)$ and $(1\bar{1}1)$ growth sectors is 1.5 mm, but, as a worst-case illustration, h will be taken as spanning the full axial height of the specimen, 3 mm. This makes $\beta_h = 3.75 \times 10^{-5}$, and $\frac{1}{2}\beta_h^2 = 7 \times 10^{-9}$, entirely negligible. On the other hand, if β_h should be superimposed on a possible $\beta = 0.3°$ due to the maladjustments considered above, then an error in relative d-spacing measurement of $\frac{1}{2}[(\beta + \beta_h)^2 - \beta^2] = 0.2 \times 10^{-6}$ would result, but is still insignificant.

Another factor is dispersion resulting from imperfect d-spacing match between the silicon and diamond reflections used. The range of ω settings, $\Delta\omega$, over which both crystals reflect when the wavelength spread is $\Delta\lambda/\lambda$ is

$$\Delta\omega = \Delta\theta_M - \Delta\theta_D = (\Delta\lambda/\lambda)(\tan\theta_M - \tan\theta_D). \quad (6)$$

Two contributions to $\Delta\lambda/\lambda$ need to be considered. First, there is a broadening of the rocking curve for all points on the specimen due to the wavelength spread resulting from the range of angles of incidence on a given point on the monochromator, $\alpha_s = (s/a)$, where s is the source dimension in the vertical plane, i.e. normal to the electron orbit. Taking the full width at half maximum intensity of s as 0.4 mm, and $a = 80$ m, gives $\alpha_s = 5 \times 10^{-6}$ and $\Delta\lambda/\lambda = \alpha_s \cot\theta_M = 1.34 \times 10^{-6}$. Then, by (6), $\Delta\omega_s = 0.077$ arcsec, too small to degrade angular resolution of the double-crystal topographs detectably. The second effect of dispersion is a shift between the centroids of rocking curves from points at the top and at the bottom of the specimen, which arises from difference in mean angles of incidence on the monochromator, and hence wavelength difference, for the rays that illuminate these top and bottom points. In this case the monochromator asymmetry enters the calculation, and the asymmetry adopted decreases the effect of dispersion. With a specimen width of 5 mm from top to bottom, the range $\Delta\omega = \omega_P(\text{bottom}) - \omega_P(\text{top})$ is 0.5 arcsec. Assuming both crystals had infinitely narrow reflection curves, the effect on the double-crystal topograph images would be for a reflecting band to pass downwards over the specimen as ω was turned to increase θ_D, simulating an overall bend of the specimen of 0.5 s. Like a real bend, its contribution to $\omega_P(1\bar{1}0) - \omega_P(1\bar{1}1)$ is eliminated by averaging measurements in the $\chi = 0°$ and $\chi = 180°$ azimuthal settings.

The last geometric factor to be considered is that arising from a difference between the actual and intended values of $2\theta_M$, which would introduce systematic error in all $\Delta d/d$ measurements. To adjust the direction of the beam reflected from the monochromator, the position of the beam over the specimen rotation axis (distant 316 mm from the monochromator rotation axis) was accurately monitored by X-ray silhouetting the tip of a pointer coincident with the specimen rotation axis. Uncertainty in the beam direction arose from uncertainty in its point of origin on the monochromator surface. By combining laser beam and X-ray beam silhouetting methods for adjusting the level of the monochromator surface every effort was made to reduce such uncertainty, and it is believed that the missetting of $2\theta_M$ was held within the limits $\pm 0.2°$. This would introduce error of $\pm\frac{2}{3}\%$ in $\tan\theta_B$, and hence in $\Delta d/d$, which is not significant compared with other uncertainties discussed below.

Turning to the second category of errors, the two scan-repetition pairs shown in figure 10 expose the worst cases of lack of reproducibility in this series of experiments. However, as table 2 indicates, they are outnumbered by cases when repeats produced indistinguishable results, or nearly so. In the case of figure 10*a*, *b* it can be seen that the scans keep quite well in step in the higher ω part of the sequence, but in the vicinity of peak reflections from {111} sectors the (*a*) sequence is compressed relative to the (*b*) sequence. The figures in table 2 suggest that on making a repeat a result differing from the first by about 0.3 arcsec might be expected, on average. It is thought that irregularities in the angular drive of the double-crystal camera were the likely source of these variations, and that they were random.

Thermal expansivities of diamond and silicon are 0.8×10^{-6} and 4.2×10^{-6} per degree respectively. The temperatures of monochromator and specimen should not change relative to each other by more than about $\frac{1}{3}°$ during the crucial part of an experiment if errors in $\Delta d/d$ are not to exceed 1 in 10^6. It is believed that the experimental routine adopted well satisfied this condition in the experiments at Station 7.6. In the case of the experiments with $\chi = 0°$ the difference in $\Delta\omega$ values between positive and negative scans suggests some drifting, but its cause is unknown.

PHILOSOPHICAL TRANSACTIONS OF THE ROYAL SOCIETY A MATHEMATICAL, PHYSICAL & ENGINEERING SCIENCES

Finally to be considered is the uncertainty, difficult to quantify, arising from errors in the subjective judgments of peak reflecting angular settings. The sequences of prints in figure 10 illustrate the problems encountered. Difficulties were lessened in practice by examining films rather than prints, using optimum viewing conditions; and all films judged had similarly well-controlled densities and contrast. It is believed that the assessments of $\omega_P\ (1\bar{1}0)$ and $\omega_P\ (1\bar{1}1)$ were each not in error by more than 0.25 s in either direction from the true value. Assuming errors in $\omega_P\ (1\bar{1}0)$ and $\omega_P\ (1\bar{1}1)$ are uncorrelated suggests probable error in $\omega_P\ (1\bar{1}0) - \omega_P\ (1\bar{1}1)$ of not more than ± 0.35 s, or $\pm 4\%$. Errors in assessing differences between $\omega_P\ (1\bar{1}0)$ and the peaks for (001) and the {113} sectors are obviously much greater. Absence of significant systematic error from diffraction-geometrical effects, or of any other origin known, leaves the variations discussed under category (ii) to be taken into account: an increase of probable error from $\pm 4\%$ to $\pm 6\%$ on their account is deemed sufficient. Thus the diffractometric measurement can be stated as

$$[a_0(1\bar{1}1) - a_0(1\bar{1}0)]/\bar{a}_0 = (1.18 \pm 0.07) \times 10^{-5}. \tag{7}$$

Regarding the {113} sectors, the topographs suggest that their nitrogen content is on the whole more uniform than would be inferred from the relatively large difference between the two infrared absorption measurements made with small probes in the $(1\bar{1}3)$ and $(\bar{1}13)$ sectors by Burns *et al.* (1990), and quoted above in §3*c*. Clearly, relative differences in a_0 of less than 1 in 10^6 are assessable from the topographs; and in this case an accuracy of about $\pm 25\%$ is attached to the finding of 0.8×10^{-6} as the average relative excess of $a_0\ (1\bar{1}3)$ and $a_0\ (\bar{1}13)$ over $a_0\ (1\bar{1}0)$. In the case of the (001) growth sector it is not known in what proportion the apparent zonal variation of a_0 is due to the variation in nitrogen content shown by figure 2 or due to constraints arising from overlap of the inner zone with the underlying $(\bar{1}\bar{1}3)$ sector, which by compressing (001) sector material in the plane (110) will cause expansion normal to (110).

(*b*) *The structure of substitutional nitrogen in diamond*

Of other experiments to measure impurity-dependent differences in the lattice parameters of different growth sectors in synthetic diamond, only two are known to the authors: those of Vishnevskii & Tkach (1982) and a contemporary study by Wierzchowski *et al.* (1991). The latter work included double-crystal topography of three large synthetic diamonds, and found values of lattice parameter differences between nitrogen-richer and nitrogen-poorer growth sectors, but their differences in infrared absorption were not known. The experiments by Vishnevskii used the divergent-beam method (Lonsdale 1947), and found a boron-doped specimen to have a_0 higher in {100} than in {111} growth sectors with the large relative difference of 5×10^{-4}.

As outlined in §1, the dilatation measurement (7) can be combined with other data to derive a figure for the effective volume of a single substitutional nitrogen atom in diamond. The first step combines the dilatation (7) with the difference in infrared absorption at 1130 cm^{-1}, $\mu(1130\ cm^{-1})$, of the growth sectors concerned using the measurements of Burns *et al.* (1990) and the re-measurement in the $(1\bar{1}1)$ sector quoted in §3*c*. It is assumed that such combination holds for all growth sectors; it gives

$$\Delta a_0/\bar{a}_0 = (2.95 \pm 0.27) \times 10^{-6}[\mu(1130\ cm^{-1})/cm^{-1}]. \tag{8}$$

The uncertainty range given in (8) is the sum of that proposed in (7) plus a cautious $\pm 3\%$ attached to the infrared absorption measurements. The second step combines

(8) with the finding of Woods *et al.* (1990) that an absorption of 1 cm^{-1} at 1130 cm^{-1} corresponds to a concentration of dispersed nitrogen of 22.0 ± 1.1 atomic parts per million. Applying this figure to the infrared absorption of the $(1\bar{1}1)$ growth sector, and subtracting the one part per million nitrogen concentration estimated by Burns *et al.* to be present in the $(1\bar{1}0)$ growth sector, gives the final result

$$\Delta a_0/\bar{a}_0 = (0.14 \pm 0.02) c_N. \tag{9}$$

Here $c_N = n_N/(n_C + n_N)$ is the fractional atomic concentration of nitrogen (n_N and n_C being numbers of nitrogen and carbon atoms per unit volume respectively), and the uncertainty of $\pm 14\%$ is the sum of that in (8) and the 5% quoted by Woods *et al.* for their measurement. Applying a simple proportionality argument, (9) can be alternatively expressed in the statement that the effective volume of a single, randomly substituted nitrogen atom is 1.41 ± 0.06 times that of the carbon atom it replaces in the diamond structure.

The finding $V_N/V_C = 1.41$ provides a datum with which to compare structures proposed for substitutional nitrogen in diamond. Most studies have considered only the extension of the unique N–C bond relative to the normal C–C bond length. From analyses of the ESR spectra Smith *et al.* (1959) concluded that an increase of 10% 'may be too high', whereas Loubser & van Wyk (1978) suggested a 10–14% extension. Different atomic cluster calculations have indicated Jahn–Teller distortions producing extensions of 26% (Messmer & Watkins 1973) and 5% to 10% (Mainwood 1979). Another Jahn–Teller distortion calculation gave 21% (Koppitz *et al.* 1986). A high value, 36%, was estimated by Ammerlaan (1981) from the frequency of reorientation of the long N–C bond by tunnelling at temperatures below 200 K. Important are the recent cluster calculations of Briddon (1990), summarized in Briddon *et al.* (1991), in which the nitrogen was surrounded by 43 carbons, the outer 36 of which had hydrogen-terminated outward-pointing bonds. The structure was determined from self-consistent pseudo-potential local density functional calculations (Jones 1988). The ratio found for unique N–C to normal C–C bond length was 1.29. A crude measure of V_N/V_C is the ratio of the volume of the tetrahedron whose apices are the four carbon atoms surrounding the nitrogen atom to that of an equivalent tetrahedron in perfect diamond. In the Briddon structure the bond lengths and angles tabulated (P. R. Briddon, personal communication) gave $V_N/V_C = 1.20$ only. However, in that model atoms in the containing shell of 36 hydrogen-terminated carbons were anchored to perfect-diamond-structure sites, allowing no expansion of the cluster as a whole. Relaxing this anchored shell in an elastic matrix will certainly increase V_N/V_C. Whether it will rise into the range 1.41 ± 0.06 will be interesting to see. What can be asserted now is that models having unique N–C bonds less than about 30% greater than the normal C–C length are in clear conflict with the dilatation measurements presented here.

The changes in the ESR spectra of type Ib diamonds observed as specimen temperature is increased show that above about 600 °C the anti-bonding electron freely re-orients among the four N–C bonds surrounding a given nitrogen atom (Shul'man *et al.* 1966; Loubser & van Ryneveld 1967). The process of incorporation of nitrogen atoms on an octahedral growth facet may well involve a stage of non-random orientation of the unique N–C bond, but this will not persist after incorporation within the bulk diamond because of thermally induced randomization. On the other hand, preferential alignment of the elongated N–C bonds is produced by uniaxial stress (Ammerlaan & Burgemeister 1980; Ammerlaan 1981). That stresses

PHILOSOPHICAL TRANSACTIONS OF THE ROYAL SOCIETY A MATHEMATICAL, PHYSICAL & ENGINEERING SCIENCES

exist between nitrogen-rich and nitrogen-poor growth sectors is abundantly shown by X-ray topography and birefringence. Koppitz *et al.* (1986) found that uniaxial stress applied along [111] induces a polarization-dependence in the absorption at 270 nm that is believed to be associated with the 1130 cm^{-1} absorption: absorption with $\boldsymbol{E}$-vector perpendicular to [111] being greater than with $\boldsymbol{E}$ parallel to [111]. In view of above findings a test was made using a grid polarizer to establish whether absorption at 1130 cm^{-1} in the $(1\bar{1}1)$ growth sector of the present specimen differed with $\boldsymbol{E}$ parallel or perpendicular to the growth surface. No difference was found. This was accepted as indicating no preferential alignment of the elongated N–C bond, no consequent loss of cubic symmetry, and thus no anisotropy in expansion due to nitrogen impurity content in this particular growth sector.

A final remark concerns the physical density of type Ib diamonds. When only one type of point defect is present in significant concentration, substitutional nitrogen in this case, physical density (i.e. ρ_w, the weighing density), lattice parameter and nitrogen concentration are not independent. Combining the last two quantities, as in (9), predicts $\Delta\rho_w/\rho_w = -0.24\, c_N$. With the laser-slicing techniques now available for excising nitrogen-rich and nitrogen-poor growth sectors from large synthetic diamonds this prediction could, and should be tested.

The authors thank the Director and Staff of the SERC Daresbury Laboratory for the provision of experimental facilities. Financial support from SERC and DeBeers Industrial Diamond Division (Pty) Ltd is gratefully acknowledged.

References

Ammerlaan, C. A. J. 1981 *Inst. Phys. Conf. Ser.*, no. 59, pp. 81–94.

Ammerlaan, C. A. J. & Burgemeister, E. A. 1980 *Ind. Diam. Rev.* **40**, 128–132.

Ando, M., Hagashi, Y., Usuda, K., Yasuami, S. & Kawata, H. 1989 *Rev. Sci. Instrum.* **60**, 2410–2413.

Bond, W. L. 1960 *Acta crystallogr.* **13**, 814–818.

Bond, W. L. & Andrus, J. 1952 *Am. Mineralogist* **37**, 622–632.

Bonse, U. 1958 *Z. Phys.* **153**, 278–296.

Bonse, U. 1965 *Z. Phys.* **184**, 71–84.

Bowen, D. K. & Davies, S. T. 1983 *Nucl. Instrum. Methods* **208**, 725–729.

Briddon, P. R. 1990 Ph.D. thesis, University of Exeter, U.K.

Briddon, P. R., Heggie, M. I. & Jones, R. 1991 In *Proc. 2nd Int. Conf. on New diamond science and technology* (ed. R. Messier, J. T. Glass, J. E. Butler & R. Roy), pp. 63–68. Pittsburgh: Materials Research Society.

Burns, R. C., Cvetkovic, V., Dodge, C. N., Evans, D. J. F., Rooney, M.-L. T., Spear, P. M. & Welbourn, C. M. 1990 *J. Crystal Growth* **104**, 257–279.

Compton, A. H. & Allison, S. K. 1935 *X-rays in theory and experiment*. New York: van Nostrand.

Davies, G. 1977 In *Chemistry and physics of carbon* (ed. P. L. Walker & P. A. Thrower), vol. 13, pp. 1–143. New York and Basel: Marcel Dekker.

Dawson, B. 1967 *Proc. R. Soc. Lond.* A **298**, 264–288.

Dyer, H. B., Raal, F. A., du Preez, L. & Loubser, J. H. N. 1965 *Phil. Mag.* **11**, 763–774.

Frank, F. C., Lang, A. R., Evans, D. J. F., Rooney, M.-L. T., Spear, P. M. & Welbourn, C. M. 1990 *J. Crystal Growth* **100**, 354–376.

Friedel, G. 1924 *Bull. Soc. fr. Minér Cristallogr.* **47**, 60–94.

Hanley, P. L., Kiflawi, I. & Lang, A. R. 1977 *Phil. Trans. R. Soc. Lond.* A **284**, 329–368.

Hart, M. 1981 *J. Crystal Growth* **55**, 409–427.

Hildebrandt, G., Stephenson, J. D. & Wagenfeld, H. 1975 *Z. Naturf.* **30**a, 697–707.

PHILOSOPHICAL TRANSACTIONS OF THE ROYAL SOCIETY A MATHEMATICAL, PHYSICAL & ENGINEERING SCIENCES

Hirsch, P. B. & Ramachandran, G. N. 1950 *Acta crystallogr.* **3**, 187–194.

Holder, D. W. & North, R. J. 1963 *Schlieren methods: NPL notes on applied science*, no. 31. London: H.M.S.O.

Jiang, S.-S., Lang, A. R. & Tanner, B. K. 1987 *Phil. Mag.* A **56**, 367–375.

Jones, R. 1988 *J. Phys.* C **21**, 5735–5745.

Kaiser, W. & Bond, W. L. 1959 *Phys. Rev.* **115**, 857–863.

Kikuta, S., Kohra, K. & Sugita, Y. 1966 *Jap. J. appl. Phys.* **5**, 1047–1055.

Koppitz, J., Schirmer, O. F. & Seal, M. 1986 *J. Phys.* C **19**, 1123–1133.

Lang, A. R. 1974 *Proc. R. Soc. Lond.* A **340**, 233–248.

Lang, A. R., Kowalski, G., Makepeace, A. P. W. & Moore, M. 1991 *Phil. Mag.* A **64**, 543–560.

Lang, A. R. & Meaden, G. M. 1991 *J. Crystal Growth* **108**, 53–62.

Lonsdale, K. 1947 *Phil. Trans. R. Soc. Lond.* A **240**, 219–250.

Loubser, J. H. N. & van Ryneveld, W. P. 1967 *Br. J. appl. Phys.* **18**, 1029–1031.

Loubser, J. H. N. & van Wyk, J. A. 1978 *Rep. Prog. Phys.* **41**, 1201–1248.

Mainwood, A. 1979 *J. Phys.* C **12**, 2543–2549.

Messmer, R. P. & Watkins, G. P. 1973 *Phys. Rev.* B **7**, 2568–2590.

Petroff, J. F., Sauvage, M., Riglet, P. & Hashizume, H. 1980 *Phil. Mag.* A **42**, 319–338.

Ramachandran, G. N. 1946 *Proc. Indian Acad. Sci.* A **24**, 65–80.

Saka, T. & Kato, N. 1968 *Acta crystollogr.* A **42**, 469–478.

Shul'man, L. A., Zaritskii, I. M. & Podzyarei, G. A. 1966 *Fiz Tverdogo Tela* **8**, 2307–2312. (English translation *Soviet Phys. Solid State* **8**, 1842–1845 (1967).)

Smith, W. V., Sorokin, P. P., Gelles, I. L. & Lasher, G. J. 1959 *Phys. Rev.* **115**, 1546–1552.

Strong, H. M. & Wentorf, R. H., Jr. 1972 *Naturwissenschaften* **59**, 1–7.

Töpler, A. 1866 *Poggendorf's Ann. Phys. Chem.* **127**, 556–580.

van Enckevort, W. J. P. & Seal, M. 1988 *Phil. Mag.* A **57**, 939–954.

Vishnevskii, A. S. & Tkach, V. N. 1982 *Sverkhtverdye Materialy*, 22–28.

Walker, J. 1979 *Rep. Prog. Phys.* **42**, 1605–1659.

Wentorf, R. H., Jr. 1971 *J. phys. Chem.* **75**, 1833–1837.

Wierzchowski, W., Moore, M., Makepeace, A. P. W. & Yacoot, A. 1991 *J. Crystal Growth*. (In the press.)

Woods, G. S. & Lang, A. R. 1975 *J. Crystal Growth* **28**, 215–226.

Woods, G. S., van Wyk, J. A. & Collins, A. T. 1990 *Phil. Mag.* B **62**, 589–595.

Received 7 March 1991; accepted 14 May 1991

PHILOSOPHICAL TRANSACTIONS OF THE ROYAL SOCIETY A MATHEMATICAL, PHYSICAL & ENGINEERING SCIENCES

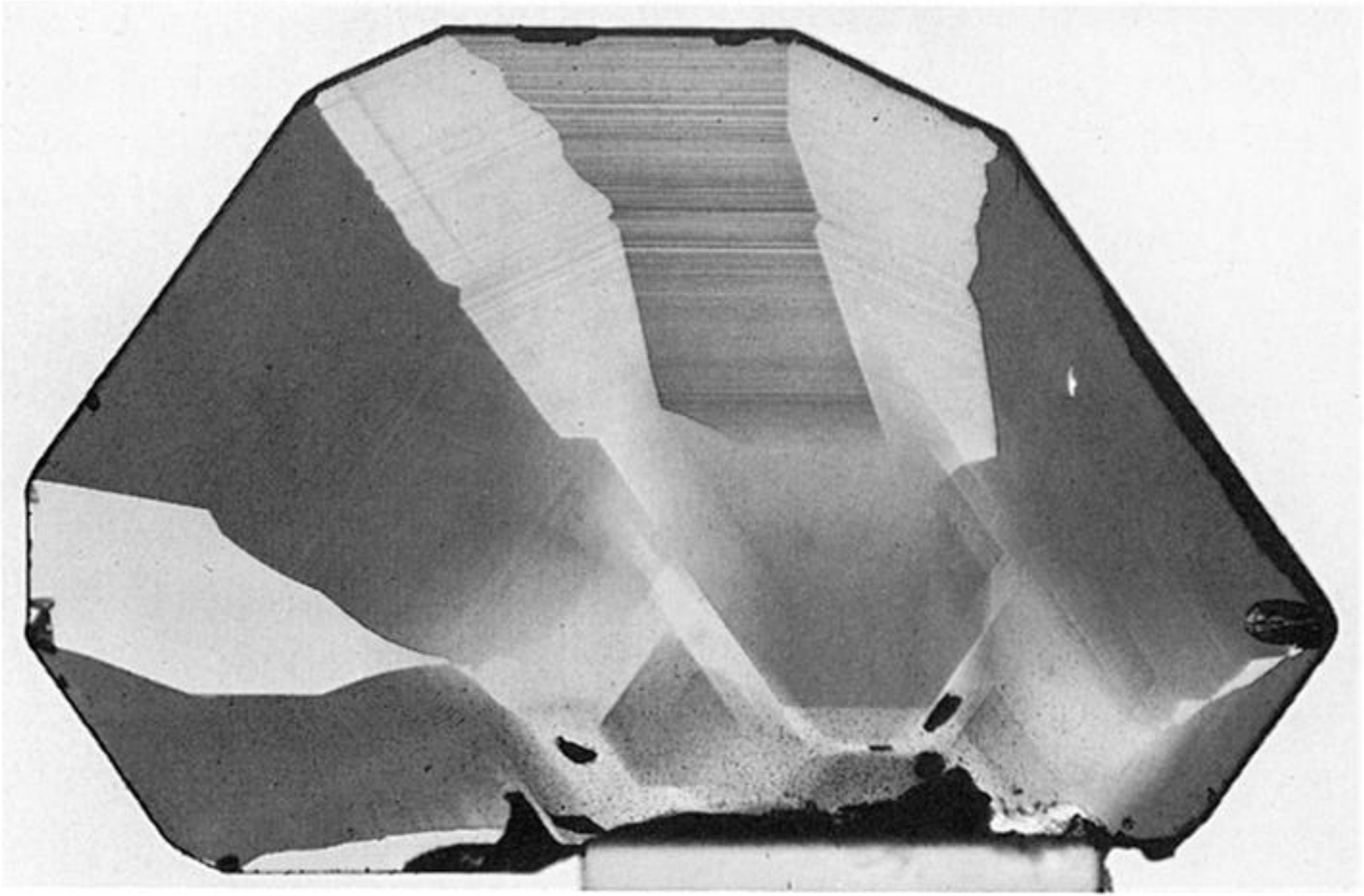

igure 2. Transmission of visible light with illumination filtered to enhance contrast between itrogen-rich sectors (dark) and sectors nitrogen-poor. Kodak-Wratten filter type 47B: peak ransmittance 50 % at 430 nm, falling to 1 % at 380 nm and 490 nm. Orthochromatic film.

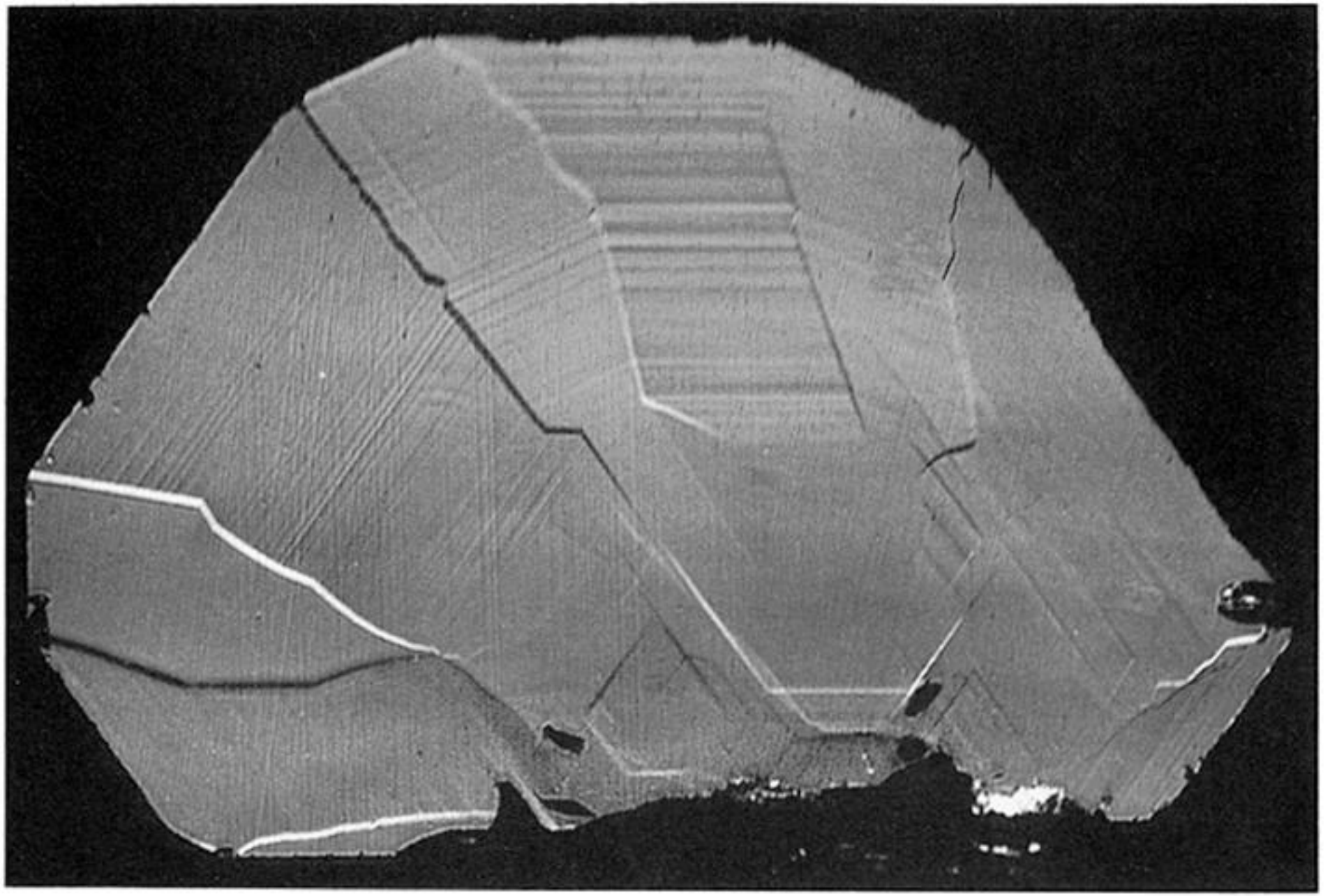

igure 3. Variations in refractive index revealed by the Schlieren pattern.

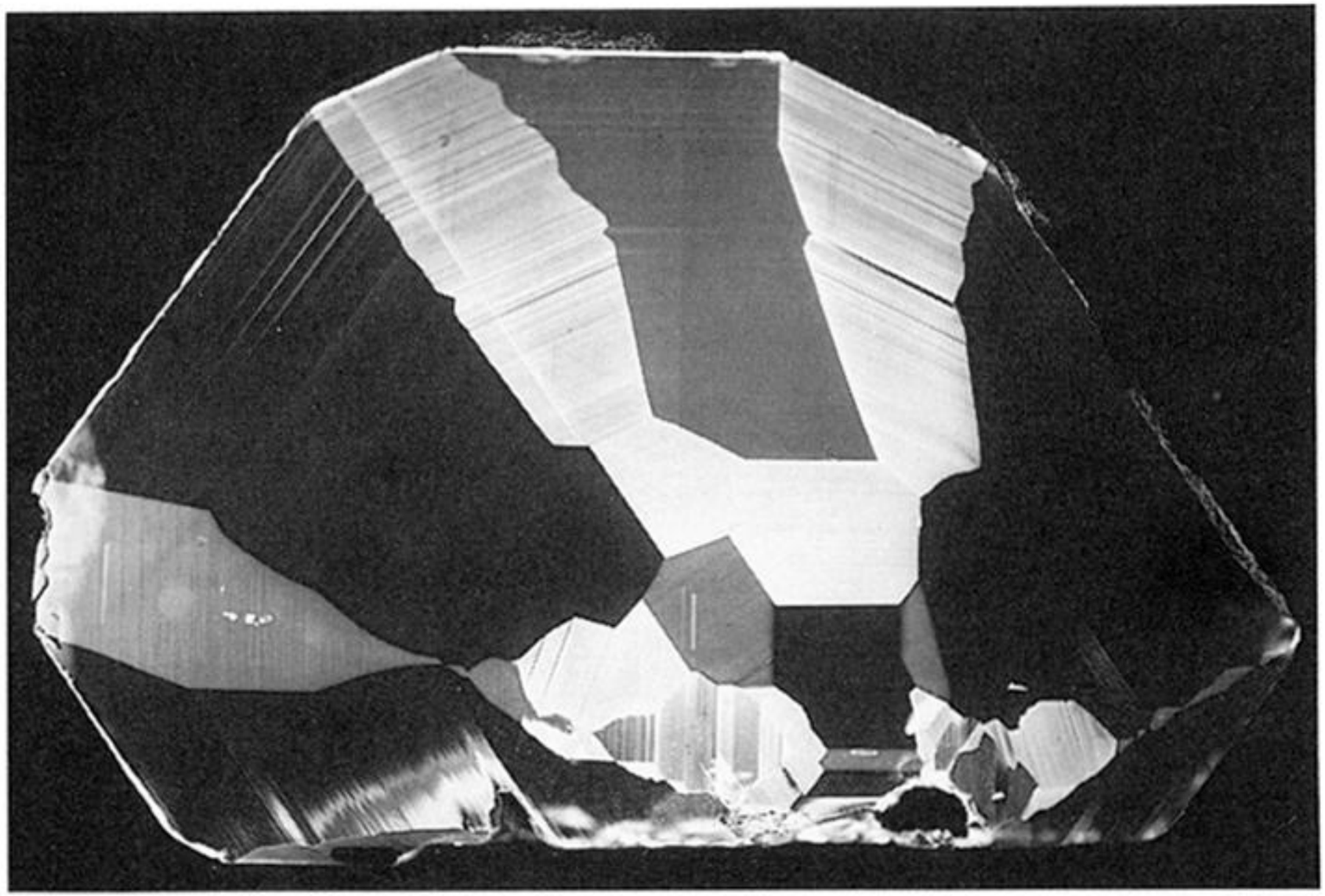

Figure 4. Room-temperature cathodoluminescence topograph of specimen surface indexed (110). Electron beam energy 40 keV, specimen current density *ca.* 1 μA mm^{-2}. Photographed through UV absorbing filter Kodak-Wratten 2B on to Kodak type 2415 extended red-sensitivity panchromatic film developed to give contrast (gamma) of *ca.* 1.

PHILOSOPHICAL TRANSACTIONS OF THE ROYAL SOCIETY A MATHEMATICAL, PHYSICAL & ENGINEERING SCIENCES

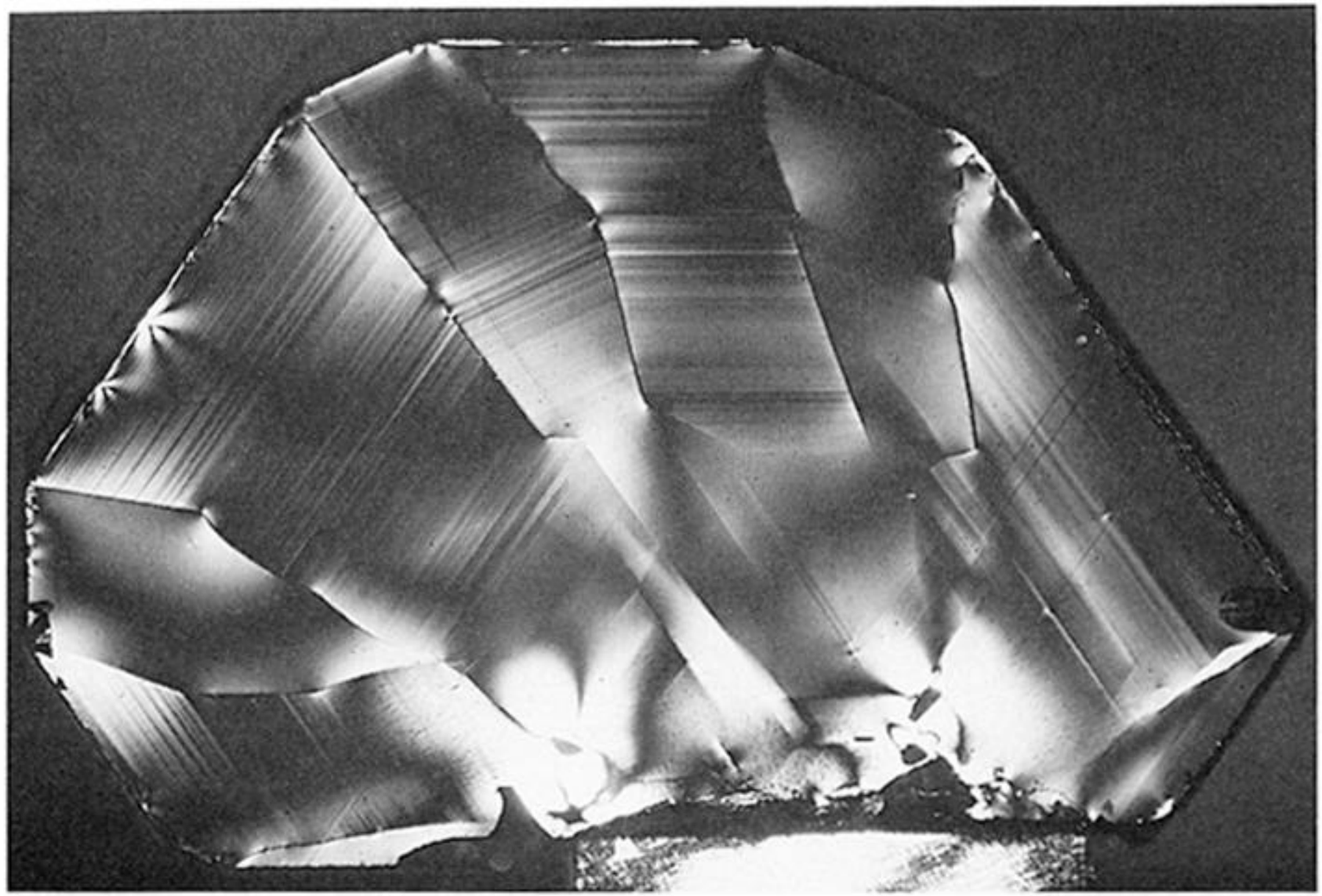

Figure 5. Birefringence pattern. Direction of view of specimen same as in figures 1–4. Axes of crossed polars parallel and perpendicular to $(\bar{1}13)$. (The specimen is supported at its lower edge by a bar of natural, plastically-deformed type IIa diamond 2 mm wide and 1 mm thick whose tip appears, strongly birefringent, at the bottom of the image.)

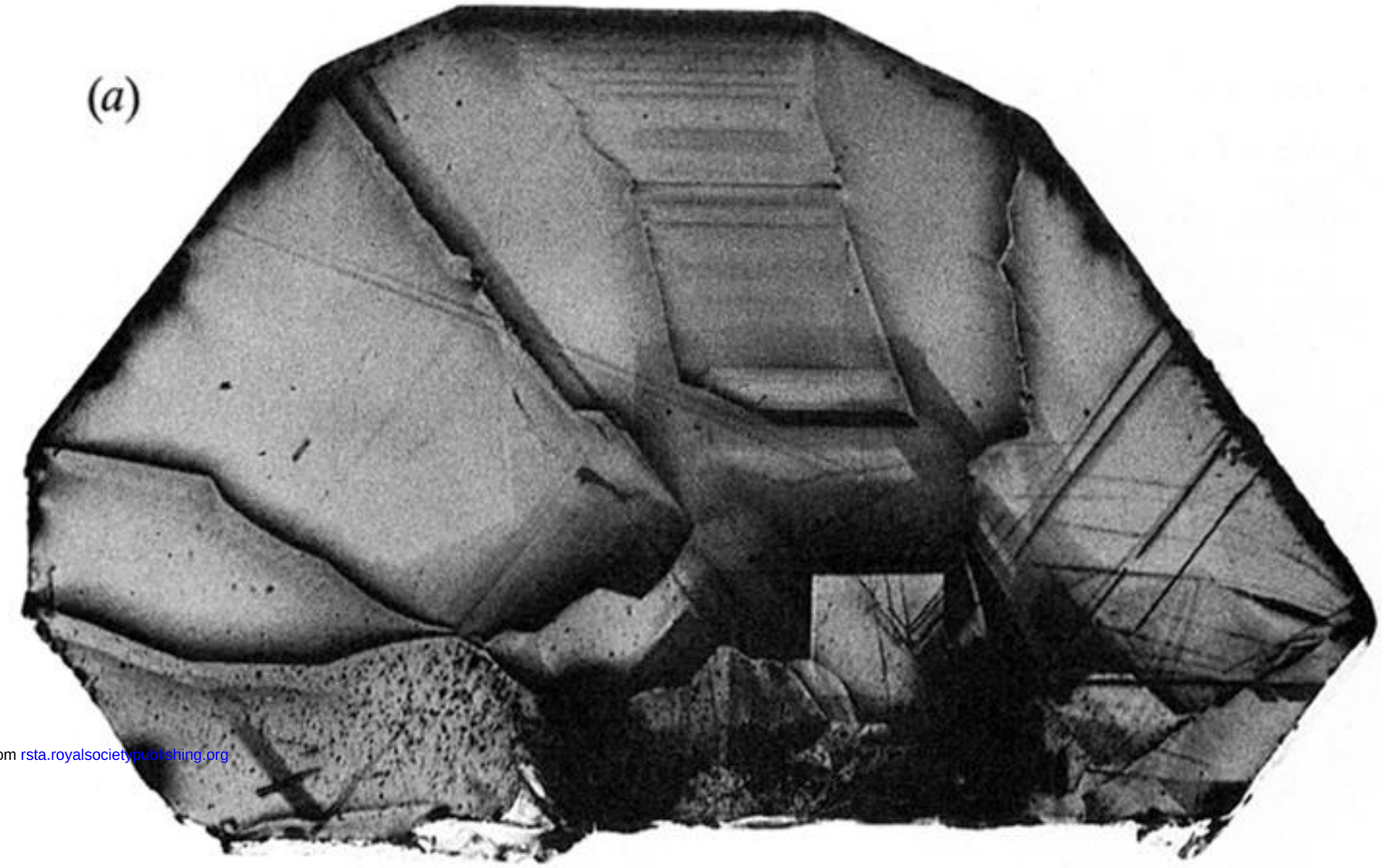

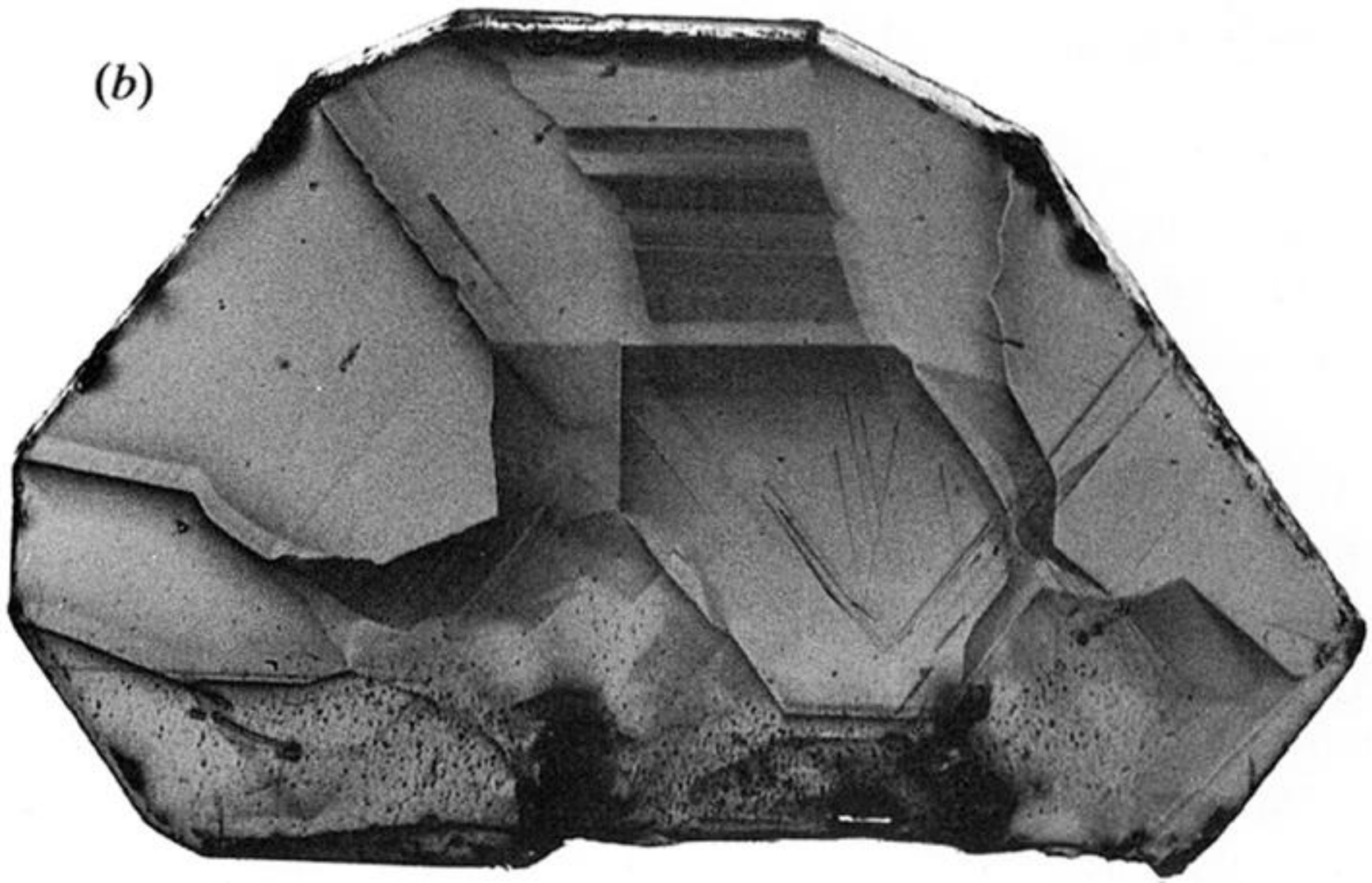

Figure 6. Reflection X-ray topographs of specimen surfaces, CuKα_1 radiation, $\lambda = 0.154$ nm, 331-type reflections, $2\theta_B = 140.5°$. Angle between incident beam and surface normal = 33°, and between surface normal and reflected beam = 6.5°. (*a*) Surface indexed (110), reflection 331. (*b*) Surface indexed $(\bar{1}\bar{1}0)$, reflection $\bar{3}\bar{3}\bar{1}$ (printed reflected in (001) for comparison with (*a*) and other figures).

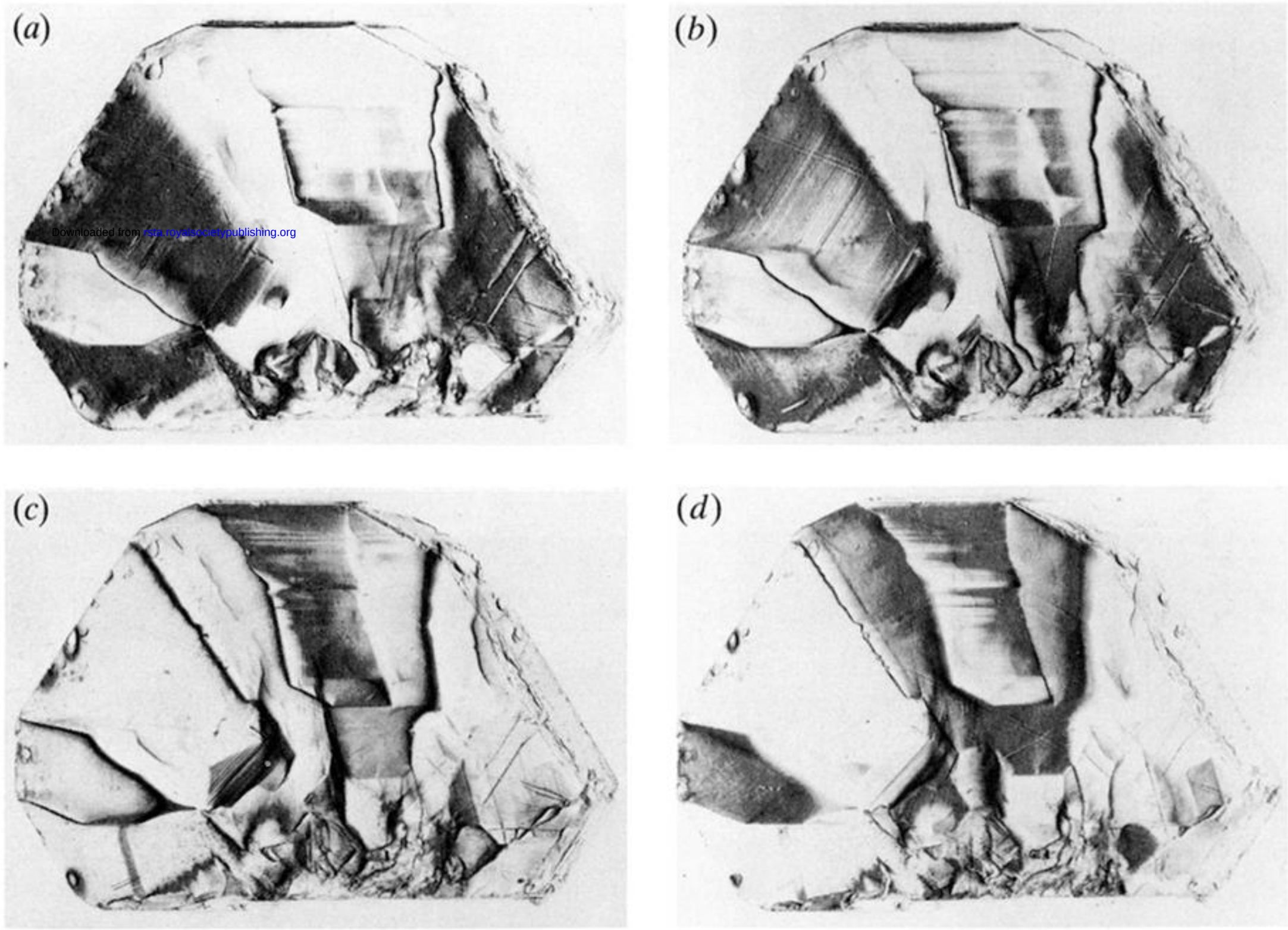

Figure 9. Members of a sequence of double-crystal topographs; silicon 175, diamond 440 reflection combination. $2\theta_M = 128°$, $\lambda = 0.113$ nm. Specimen glancing angle ω increasing in *ca.* 1 arcsec steps from (*a*) to (*d*). Azimuthal angle $\chi = 180°$, in which setting the plane of incidence is (001) and the diffracted beam leaves the crystal in a direction rotated 25.5° from the surface normal towards [110] (allowing for $\approx 1°$ difference between [110] and the surface normal). Horizontal foreshortening factor 0.9. Ilford nuclear plates type L4, exposures *ca.* 100 mA minutes electron beam current.

PHILOSOPHICAL TRANSACTIONS OF THE ROYAL SOCIETY A MATHEMATICAL, PHYSICAL & ENGINEERING SCIENCES

Figure 10. Sequences of double-crystal topographs recorded with $2\theta_M = 150°$, $\lambda = 0.121$ nm, ω increasing in nominal 1 arcsec steps from top to bottom. Recorded on Agfa-Strukturix D7 film, exposures *ca.* 70 mA minutes. (*a*) $\chi = 180°$, diffraction geometry similar to figure 9, but view of specimen surface less oblique (film 1*). (*b*) Repeat of (*a*) (film 5*). (*c*) $\chi = 0°$, image rotated 180° in its own plane for comparison with (*a*) and (*b*), so that the specimen viewing direction is from left of the surface normal (film 1). (*d*) Repeat of (*c*) (film 5).